RÚBEN ALEXANDRE BASTOS GOMES

BIOCOMPATIBLE TI ALLOYS POROUS STRUCTURES MANUFACTURED BY LASER POWDER BED FUSION FOR ORTHOPEDIC IMPLANTS

Dissertation to obtain the Master of Science Degree in Biomedical Engineering

SUPERVISOR

Professor Doctor Maria João Pedroso Carmezim

Professor Doctor Rodolfo Lisboa Batalha

October 2025

RÚBEN
ALEXANDRE
BASTOS GOMES

BIOCOMPATIBLE TI ALLOYS POROUS STRUCTURES MANUFACTURED BY LASER POWDER BED FUSION FOR ORTHOPEDIC IMPLANTS

EXAMINATION COMMITTEE

Chairperson: Prof. Doctor Célio Gabriel Figueiredo Pina, Polytechnic Institute of Setúbal
Supervisor: Prof. Doctor Maria João Pedroso Carmezim, Polytechnic Institute of Setúbal
Supervisor: Prof. Doctor Rodolfo Lisboa Batalha, Welding and Quality Institute
Vogal: Prof. Doctor Catarina Ferreira dos Santos, Polytechnic Institute of Setúbal

October 2025

“Living is facing one problem after another. How you face it is what makes the difference.”

— Benjamin Franklin

Acknowledgments

Firstly, I would like to express my deepest gratitude to my family for their unconditional support and constant motivation every time in my life. They have been, and continue to be, my solid foundation and my greatest inspiration.

To my colleagues at the IPS E122 laboratory, to whom I now consider true friends, I offer my very special thanks. Your companionship, help and encouragement have been fundamental along this journey, making each challenge easier and each achievement more meaningful.

To my supervisor, Professor Maria João Carmezim, I express my sincere gratitude for her vote of confidence, for the way she has always encouraged me to see the positive side of situations, and for the honesty and dedication she has always shown. Her guidance was essential to my personal and academic growth.

To my supervisor, Professor Rodolfo Lisboa Batalha, I extend my special thanks for his tireless commitment, constant availability, and patience in clarifying even the simplest questions. His dedication and rigor were fundamental to the completion of this work and allowed me to evolve both as a professional and as a person.

To my colleagues at the Institute of Welding and Quality (ISQ), I am grateful for making every day at work lighter and more enjoyable, for the spirit of mutual support and for the positive environment you created.

To all those who, directly or indirectly, contributed to the completion of this stage, thank you so much.

This work is part of the Project S0737 ADAPT - Digital Manufacturing of Customized Orthopaedic Implants, which received funding from Agencia Nacional de Inovação (ANI) in the Eureka and the Clusters program and SMART Cluster through COMPETE2030-FEDER-01654300.

Resumo

Ligas biocompatíveis de Ti puro, Ti-6Al-4V ELI e Ti-39Nb foram produzidas por Fusão a Laser em cama de pó com geometrias maciças, gyroids e Voronoi, seguidas de caracterização microestrutural e mecânica. Os resultados mostraram que a liga Ti-39Nb tem maior ductilidade e um módulo de elasticidade mais próximo do osso cortical (E = 77 ± 2 GPa , $\sigma_{máx}$ = 754 ± 18 MPa, $\varepsilon_{máx}$ = 19 ± 3 %) apresentando elevado potencial para reduzir o efeito de blindagem de tensão em implantes ortopédicos, enquanto o Ti-6Al-4V revelou maior rigidez (E = 109 ± 1 GPa, $\sigma_{máx}$ = 1165 ± 53 MPa, $\varepsilon_{máx}$ = 10 ± 1 %) e resistência mecânica com menor comportamento dúctil. As geometrias gyroids demonstraram melhor desempenho do que as Voronoi, sugerindo maior potencial para aplicações biomédicas.

Palavras-chave: Manufatura Aditiva, Fusão a Laser em Cama de Pó, Ligas de Titânio, Estruturas Porosas, Implantes Ortopédicos.

Abstract

Biocompatible alloys of pure Ti, Ti-6Al-4V ELI, and Ti-39Nb were produced by powder bed laser melting with solid, gyroid, and Voronoi geometries, followed by microstructural and mechanical characterization. The results showed that the Ti-39Nb alloy has greater ductility and a modulus of elasticity closer to that of cortical bone ($E = 77 \pm 2$ GPa , $\sigma_{max} = 754 \pm 18$ MPa, $\varepsilon_{max} = 19 \pm 3\%$), showing high potential for reducing the stress shielding effect in orthopedic implants, while Ti-6Al-4V revealed greater stiffness ($E = 109 \pm 1$ GPa, $\sigma_{max} = 1165 \pm 53$ MPa, $\varepsilon_{max} = 10 \pm 1$ %) and mechanical resistance with less ductile behavior. Gyroid geometries demonstrated better performance than Voronoi ones, suggesting greater potential for biomedical applications.

Keywords: Additive Manufacturing, Laser Powder Bed Fusion, Titanium alloys, Porous Structures, Orthopedic implants.

Contents

List of Figures

List of Tables

List of Abbreviations

Al	Aluminum
AM	Additive Manufacturing
ASTM	American Society for Testing and Materials
BCC	Body Center Cubic
BSE	Backscattered Electrons
CAD	Computer Assisted Design
CP-Ti	Commercially pure Titanium
DIC	Digital Image Correlation
EDS	Energy Dispersive X-ray Spectroscopy
ELI	Extra Low Interstitial
EN	European Norm
Gr 23	Grade 23
HCP	Hexagonal Close-Packed
ISO	International Organization for Standardization
IST	Instituto Superior Técnico
L-PBF	Laser Powder Bed Fusion
Nb	Niobium
NP	Portuguese Norm
OM	Optical Microscopy
PLA	Polylactic Acid
RPM	Rotation per minute
SE	Secondary Electrons
SEM	Scanning Electron Microscope
SLA	Stereolithography
Ta	Tantalum
Ti	Titanium
TNZT	Ti-35Nb-7Zr-5Ta
UTM	Universal Testing Machine

UTS	Ultimate Tensile Strength
V	Vanadium
XRD	X-ray Diffraction
XRF	X-ray Fluorescence Spectrometry
Zr	Zirconium
YS	Yield Strength

List of Symbols

α	Alpha Phase
α`	Alpha Prime Phase
α``	Alpha Double Prime Phase
β	Beta Phase
ε	Elongation
σUTS	Ultimate Tensile Strength
σYS	Yield Strength
б	Standard Deviation
E	Young's modulus
GPa	Gigapascal
H2O	Water
HF	Hydrofluoric acid
HNO3	Nitric acid
Kg	Kilogram
kN	Kilo Newton
kV	Kilo Volt
m	Mass
m3/h	Cubic meter per hour
mm	Millimeter
mm/min	Millimeter per minute
MPa	Mega Pascal
p	Sanding paper grit size
ppm	Parts per million
W	Watt
ρ	Density
%	Percentage
°C	Degree Celsius
g/m3	Gram per cubic meter

μm	Micrometer

Chapter 1
Introduction

This chapter introduces the topic of this thesis by explaining its motivation, defining the research problem, and outlining the key objectives that directed the development of the proposed solution. In addition, it provides a concise overview of the thesis structure and organization.

1.1. Motivation

One of the main reasons for the growing demand for advanced solutions in the field of materials and biomaterials stems from the need to improve the quality and longevity of medical implants. Despite the widespread use of the Ti-6Al-4V alloy, it has limitations, such as the significant difference between its modulus of elasticity and that of human bone, leading to stress shielding phenomena and compromising long term bone integration. Beta (β) titanium alloys, particularly those of the Ti-Nb system, emerge as a promising alternative due to their high biocompatibility, corrosion resistance and mechanical properties closer to those of bone tissue. The application of additive manufacturing technology, namely Laser Powder Bed Fusion (L-PBF), also allows the development of complex geometries and biomimetic structures, enabling customized implants that promote bone regeneration and integration. Thus, the study of these alloys is of high scientific and technological relevance, contributing to significant advances in the field of biomedical engineering, which is what motivated this master’s thesis.

1.2. Problem statement

Functional impairment of tissues is the main cause that forces thousands of patients to resort to implants. This factor can be triggered by various causes such as trauma or accidents, degenerative diseases, ageing, among others. It is estimated approximately 116.900 hip procedures and approximately 134.650 knee procedures according to the 2024 report from the UK National Joint Registry (National Joint Registry, 2024). The main problem underlying the application of orthopedic implants is called stress shielding and occurs when the rigidity of the implant is much greater than that of the adjacent bone, causing it to deviate and reduce the mechanical loads that would normally be supported by the bone. This causes the bone to lose mechanical stimulation and resorb (Wolff's law), leading to a decrease in bone density. Implant loosening may occur over time requiring revision surgery, where the chances of success are less than a normal surgery (Akhtar et al., 2025).To tackle this challenge, the current work investigates the effect of different engineered porous structures on the microstructural and mechanical characteristics of biocompatible and commercially available titanium alloys and a beta Ti-Nb alloy, which has a lower Young's modulus than the traditionally used Ti-6Al-4V alloy. The materials are processed by laser powder bed fusion (L-PBF). With the aim of reducing implant stiffness and promote a more favorable osseointegration, two geometries (Voronoi and gyroid) with three different levels of porosity (50%, 65% and 75%) were studied.

1.3. Research objectives

The main objective of this work is to study the microstructural and mechanical characteristics of biomedical titanium alloys produced by laser powder bed fusion (L-PBF) with engineered porous structures. Three biocompatible materials are considered: commercially pure Ti (Grade 2), Ti-6Al-4V ELI (Grade 23), and Ti-39Nb. The work focuses on bulk, gyroid and Voronoi geometries, with the aim of improving biomechanical compatibility for potential implant applications. The specific objectives of the study are:

- Design of engineered porous structures: Develop cylinders with gyroid and Voronoi unit cells.
- Evaluation of feedstock powders: Characterize the metallic powders used as raw materials in L-PBF.
- Production of bulk and porous materials: Manufacture cylindrical specimens of pure Ti, Ti-6Al-4V ELI and Ti-39Nb alloys using L-PBF with bulk and porous geometries.
- Microstructural and mechanical characterization: Analyze the microstructure and mechanical properties (stiffness, tensile and compressive strength) and potential biomechanical compatibility of the materials and geometries.

1.4. Document organization

This thesis is structured into five chapters, each addressing specific aspects of the research in a logical and coherent sequence. Chapter 1 introduces the work by presenting its motivation and scientific relevance, outlining the problem to be addressed, and establishing the objectives that guided the study. It also provides a detailed explanation of the scope and structure of the thesis, clarifying how the chapters are interconnected.

Chapter 2 presents a literature review, covering the theoretical and scientific background necessary to contextualize the research. Emphasis is placed on Ti alloys, with a focus on the β-Ti alloys and the specific case of the Ti-Nb system manufactured by L-PBF. Furthermore, this chapter includes a comparative analysis between the characteristics of cortical bone and Ti-6Al-4V, Pure Ti, and Ti-39Nb alloys, as well as a discussion on porous and lattice structures designed for biomedical implants.

Chapter 3 describes the materials and methodologies adopted in the experimental phase. It includes the preparation of samples for subsequent analyses, the design of test geometries, and the fabrication process through additive manufacturing. Emphasis is given to ensuring methodological rigor, reproducibility, and alignment with the objectives established. Description of the experimental techniques employed for the characterization of the materials are included into this chapter. This includes both microstructural analysis techniques (optical microscopy, scanning electron microscopy and X-ray diffraction) and mechanical testing procedures, with an explanation of the principles behind each technique and the justification for their selection.

Chapter 4 presents and discusses the results obtained throughout the experimental work. The findings are analyzed in detail and interpreted considering the literature review presented in Chapter 2, allowing a critical comparison with previous studies. The discussion highlights both the achievements of the study and its limitations, identifying possible reasons for deviations and outlining their implications.

Chapter 5 summarizes the main conclusions derived from the research. This chapter highlights the contributions of the thesis to the field of Biomedical Engineering, emphasizing the scientific and practical significance of the results. Additionally, it outlines perspectives for future works, suggesting possible directions for continued research.

Chapter 2
Literature Review

This chapter presents the research undertaken to establish theory foundation and to inform the experimental work of this thesis. It critically examines existing knowledge in the field while highlighting key insights and potential avenues for future investigation.

2.1. Beta Ti alloys

Titanium alloys consist of a material composed mainly of Ti with the addition of chemical elements to improve specific properties, depending on the purpose of the application (Nadammal et al., 2022; L.-C. Zhang et al., 2023). The Ti alloys present two main crystalline phases: the alpha (α) phase and the beta (β) phase, the latter being specifically important for biomedical applications (R. L. Batalha et al., 2022; L.-C. Zhang et al., 2023).

The β-phase in pure titanium is the body-centered cubic (BCC) crystal structure stable at temperatures above 882ºC, which is the so-called β-transition temperature (Nadammal et al., 2022; Rehman et al., 2023). Below this temperature, the structure of pure Ti undergoes a structural change, moving from the high temperature β phase to the lower temperature α phase with hexagonal close-packed (HCP) crystalline structure (Nadammal et al., 2022; Rehman et al., 2023). In the β phase, the atoms are organized in such a way that there is an atom in the center of the cube and an atom at each vertex of the cube of the BCC structure. This organization allows for the formation of different sliding planes (surfaces where the atomic layers can slide over each other), making it possible to respond adaptively to applied stresses (Zou et al., 2024a). When faced with cyclical loads, the planes rearrange and dissipate localized stresses, reducing their accumulation at specific points (Zou et al., 2024a). The beta phase in titanium alloys have several advantages for applications that require a balance between flexibility and strength (such as orthopedic implants) as illustrated in Figure 2.1 (Nadammal et al., 2022; Rehman et al., 2023; L.-C. Zhang et al., 2023; Zou et al., 2024a).

Beta-Ti alloys have greater ductility and malleability compared to α-Ti alloys, making them easier to deform plastically and to be molded into complex geometries without losing their structural strength (L.-C. Zhang et al., 2023; Zou et al., 2024a). Furthermore, this type of alloy has a modulus of elasticity (or Young's modulus) significantly lower than the α-Ti alloys and closer to that of cortical bone, which significantly reduces the effects of stress shielding and thus improves bone integration (L.C. Zhang et al., 2023).

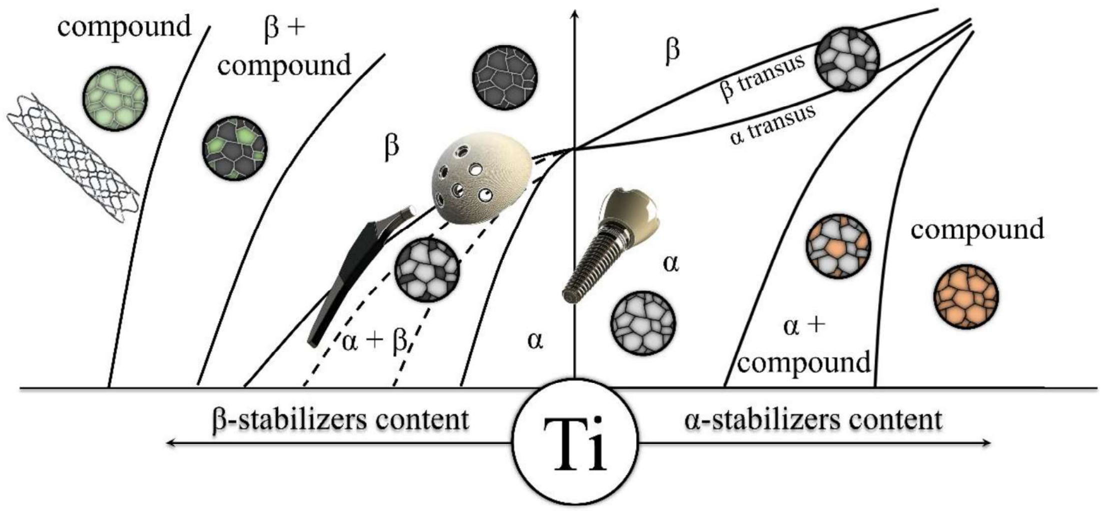

Figure 2.1 - Schematic phase diagram of titanium alloys representing the relationship of phase stabilizer additions and biomedical components (Marin & Lanzutti, 2024).

Although the β phase in Ti alloys has coveted characteristics for biomedical applications, this phase is not naturally stable at room temperature in pure Ti. Therefore, to ensure that the β-phase remains stable and has its advantageous properties under this condition, specific elements called β-stabilizers must be added (as can see in Figure 2.2) (Zou et al., 2024a). This group of elements is divided into two categories, strong β-phase stabilizers and moderate β-phase stabilizers (Zou et al., 2024a). Strong β-phase stabilizers consist of elements such as niobium (Nb), molybdenum (Mo) and tantalum (Ta) that reduce the β-transition temperature abruptly and allow the β-phase to be retained at room temperature (as can see in Figure 2.3) (L.B. Zhou et al., 2021). Moderate β-phase stabilizers consist of elements such as zirconium (Zr) and tin (Sn) which help to reduce the β-transition temperature, but to a less extent (Kong et al., 2021a).

The addition of β-phase stabilizers Nb, Zr and Ta as alloying elements play specific roles in stabilizing the β phase and optimizing mechanical and corrosion properties, as can be seen in Figure 2.2 (Nadammal et al., 2022; Rehman et al., 2023). Niobium (Nb) acts as a strong stabilizer of the β phase, lowering the transition temperature and allowing the alloy to retain this structure even at room temperature. This gives the alloy greater flexibility and strength, suitable for withstanding dynamic loads in implants (such as locomotion). Zirconium (Zr) acts as a moderate stabilizer of the β phase, improving corrosion resistance without compromising the alloy's ductility. It also reduces the modulus of elasticity, bringing it closer to cortical bone, which minimizes the stress shielding effect (Kong et al., 2021a, 2021b; Moffat & Kattner, 2020.). Tantalum (Ta) strongly stabilizes the β phase and gives the alloy excellent chemical resistance and biocompatibility. As it is inert, it helps protect the alloy against corrosion, which is essential for the physiological environment (L.-B. Zhou et al., 2021).

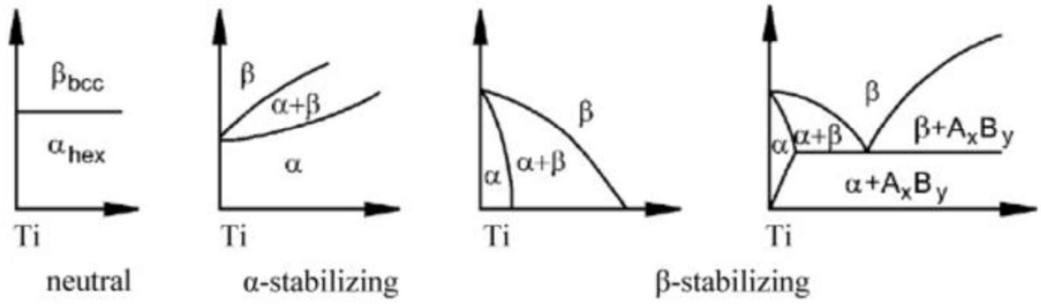

Figure 2.2 - Influence of selected alloying elements on the phase stability of titanium alloys (Huber et al., 2021)

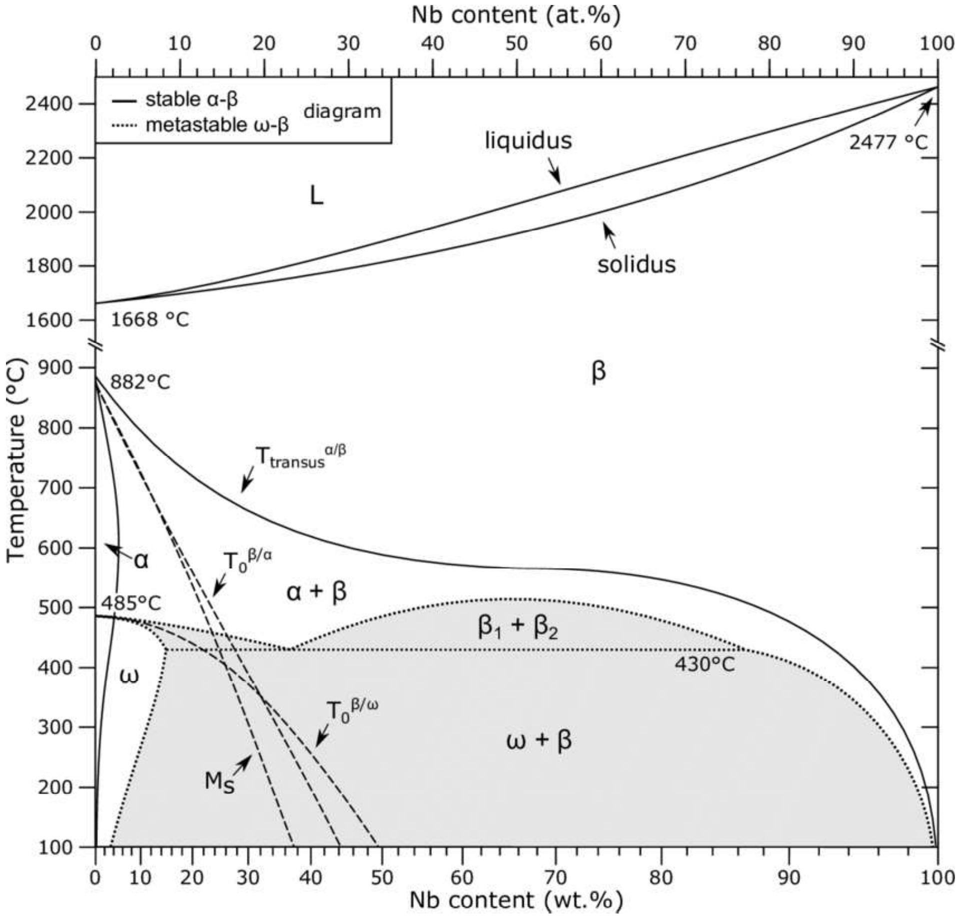

Figure 2.3 – Diagram of Nb content in Ti-Nb alloys(Bönisch, 2016.)

Titanium is a reactive metal with high affinity to oxygen and, therefore, a very stable layer of Ti oxide (TiO2) forms in Ti-based alloys, which adheres perfectly to implant surfaces and prevents chloride ions (Cl) that are the main culprits in corrosion (L.-C. Zhang et al., 2023). In this way, it can be said to have excellent resistance to corrosion. Furthermore, when beta-stabilizers are added in β-Ti alloys, corrosion resistance is enhanced, especially when elements such as Nb and Ta are present, since they form very stable oxides in the material surface that acts as an important protective barrier for corrosion, contributing to the high chemical stability of the beta-Ti alloy, which consequently leads to improved electrochemical resistance (Kong et al., 2021a; L.-C. Zhang et al., 2023; L.-B. Zhou et al., 2021).

Compared to the Ti-6Al-4V alloy often used in medical implants, the Ti-Nb alloys have several advantages. According to (Tardelli et al., 2024a), since toxic elements such as aluminum and vanadium are not in the chemical composition of Ti-Nb alloys, they are more biocompatible. These alloys show high resistance to corrosion and biocompatibility, essential factors for the durability of implants in the human body without jeopardizing the patient's health (Tardelli et al., 2024a; L.-C. Zhang et al., 2023). Furthermore, it has been reported that Ti-Nb alloys such as the Ti-39Nb has a modulus of elasticity of 44-89 GPa, which is closer to that of cortical bone (10-30 GPa) (Tardelli et al., 2024a).Therefore, the Ti-39Nb, which is a well-known biocompatible alloy where beta phase can be obtained at room temperature is investigated in the present work and compared to pure Ti and Ti-6Al-4V alloy.

2.2. Comparison of cortical bone with Ti alloys

The human body is made up of 206 bones, each of which is divided into two parts – trabecular and cortical (Evans, 1980.). Cortical bone is the hard outer part of the bone structure and is mainly made up of an organic matrix (type I collagen) and inorganic components (such as hydroxyapatite and other minerals). It has a very viscoelastic structure (ability to deform and return to its place) and is anisotropic (mechanical properties vary according to direction). In the field of medical implants, cortical bones are used to compare the natural mechanical properties of bone with those of the artificial materials used (mainly metallic) in implants (Y. Ma et al., 2024).

When human bones are healthy, its modulus of elasticity (or Young's modulus) varies between 10-30 GPa (Tardelli et al., 2024a; L.-C. Zhang et al., 2023). The most widely used Ti alloy is the Ti-6Al-4V, which normally has a modulus of elasticity of 110 GPa, while the Ti-Nb alloys manufactured by L-PBF has a modulus of elasticity between 44-89 GPa (L.-C. Zhang et al., 2023). On the other hand, the tensile strength offered by cortical bone varies between 68-132 MPa, while the Ti-6AL-4V alloy has values of around 960 MPa and the Ti-39Nb has values of between 670-770 MPa, as can be seen in Table 2.1 (J. C. Wang et al., 2022; L.-C. Zhang et al., 2023).

Table 2.1 - Mechanical properties of cortical bone and Ti alloys (Adapted from Tardelli et al., 2024 and L.C. Zhang et al., 2023).

Materials	Manufacturing	E (GPa)	$\sigma_{máx}$ (MPa)	$\varepsilon_{máx}$ (%)
Cortical Bone	-------	10-30	68-132	-----
Ti-6Al-4V	L-PBF	110	941	10 ± 1.2%
Ti-39Nb	L-PBF	44-89	670-770	16.5 ± 1.8%

In terms of biocompatibility, Ti-Nb alloys such as Ti-39Nb alloy have advantages over Ti-6Al-4V due to the absence of toxic elements in its composition such as aluminum and vanadium. Furthermore, the fatigue resistance of Ti-Nb is high enough to ensure long service life of the implants (R L Batalha et al., 2022; Tardelli et al., 2024; L.-C. Zhang et al., 2023).

As for density, cortical bone has values ranging from 1.8-2.0 g/cm^3, whereas Ti-6Al-4V is a lightweight alloy with density of 4.5 g/cm^3, while the Ti-39Nb alloy, after applying some porosity such as Voronoi or gyroid geometries, can reach a density very close to that of cortical bone (Huber et al., 2021).

By analyzing the data, it is to be expected that Ti-Nb alloys have a better mechanical compatibility, due to a modulus of elasticity closer to that of bone, being less prone to worsening levels of stress shielding, combine with a higher level of biocompatibility, not only due to the absence of toxic chemical elements but also the engineered porosity enable by the L-PBF process. The engineered porosity makes it easier for cells to adhere to the surface, create a community and proliferate, which will accelerate bone growth repair (L.-C. Zhang et al., 2023).

2.3. Laser powder bed fusion

Laser powder bed fusion (L-PBF) is a metal additive manufacturing (AM) technology that melts metallic powders layer by layer using a fiber laser to produce complex parts, such as Voronoi or gyroid geometries. The systems consist of a laser source that emits a beam with 50-1000 Watts. The laser beam is directed by a galvanometer in such a way as to control its trajectory (Ibrahim et al., 2024). The powder is spread onto the substrate by a *recoater* forming a powder bed, which is scanned by the laser beam that melts the powder according to the cross-section of the CAD geometry. The platform is then lowered by a pre-defined layer thickness (0.02-0.12 mm) in a closed chamber protected by argon, nitrogen or helium, as can be seen in Figure 2.4.

The basic process parameters are laser power, scanning speed, layer thickness, hatching distance, and scanning strategy (W. C. Batalha et al., 2023a). The process has several advantages, such as manufacturing parts with a high level of complexity and resolution, allowing the creation of functional parts with engineered porosities and with complex and personalized designs, without the need for molds or tools. Furthermore, only the necessary amount of material to produce the part is used, leading to minimum material waste. Therefore, L-PBF has emerged as an affordable manufacturing route for small and medium-sized parts (Chowdhury et al., 2022; Oliveira et al., 2020). On the other hand, it also has some disadvantages such as high equipment and material costs (in terms of acquisition), low manufacturing production rate, low degree of reproducibility, the need for post-processing, high residual stresses in the parts (due to rapid heating and cooling), limitations in terms of the size of the parts that can be produced and the need for suitable facilities (due to operating in a controlled environment) (W. C. Batalha et al., 2023a; Chowdhury et al., 2022; Oliveira et al., 2020; Schulze et al., 2018; Sefene, 2022; Zou et al., 2024b).

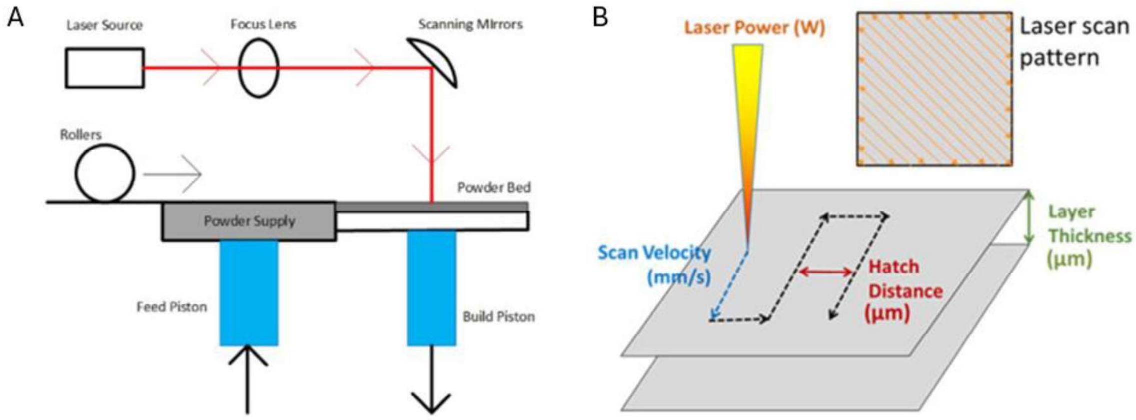

Figure 2.4 - A) Typical operation diagram of an L-PBF machine (Chowdhury et al., 2022); B) Common process parameters in laser powder bed fusion (Oliveira et al., 2020).

2.4. Ti-Nb alloys produced by Laser Powder Bed Fusion

In the past five years, β-phase titanium alloys produced through Laser Powder Bed Fusion (L-PBF) have gained increasing relevance within the biomedical field, representing a significant part of the global study of beta phase Ti alloys, a trend that is clearly reflected in the accompanying graph with a database from ScienceDirect platform, as can be seen in Figure 2.5.

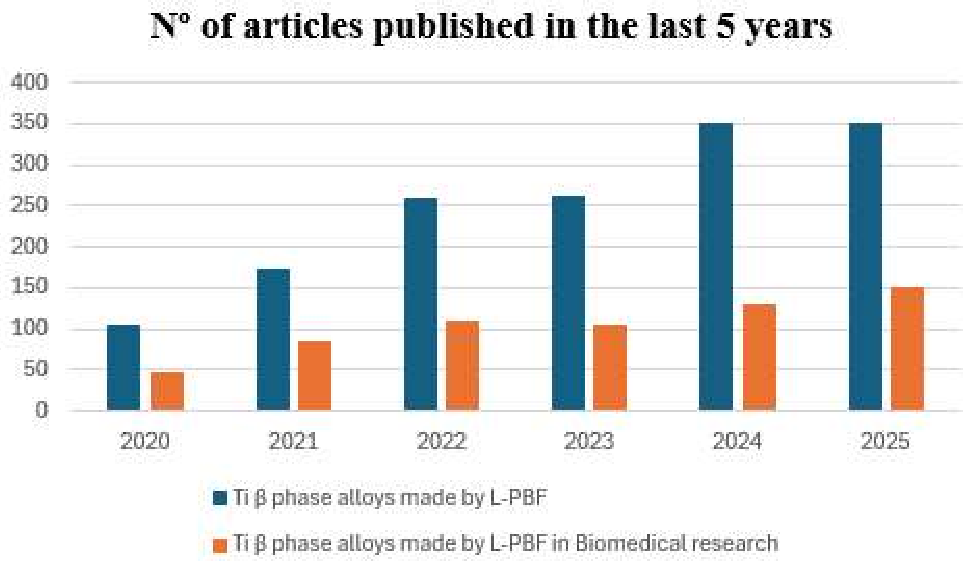

Figure 2.5 - Graph referring to the number of articles published in the last 5 years about Ti β phase alloys in general and in biomedical field.

These alloys have attracted considerable attention for biomedical applications, mainly because they offer a favorable combination of mechanical strength, low stiffness (elastic modulus) and excellent biocompatibility, desirable characteristics for implants that minimize the *stress shielding* effect. The Laser Powder Bed Fusion (L-PBF) additive manufacturing process allows to produce complex geometries with high control of microstructure and associated high cooling rates, which are rare in conventional methods, paving the way for unique microstructures. The high cooling rate inherent to the L-PBF process favors the solidification of the metastable β phase in Ti-Nb alloys refined cellular or dendritic microstructure, although the presence of martensitic α″ phase is often observed (Hafeez et al., 2021). The Nb content plays a central role: high Nb values stabilize the β phase down to room temperature, minimizing the formation of α″.

Ti-Nb alloys produced by LPBF have demonstrated significantly lower Young's moduli than conventional alloys such as Ti-6Al-4V, which favors mechanical adaptation to bone. (Stefan Pilz et al., 2022), it was possible to achieve a modulus as low as 44 GPa along the build direction, while maintaining a high yield strength of 674 MPa for a texture-controlled Ti-42Nb alloy. Comparisons of tribocorrosion and microenvironmental behavior also show that Ti-Nb can form more stable oxides (thanks to Nb), resulting in greater resistance to corrosion or tribocorrosion, which is useful in implants exposed to body fluids/mechanical wear. (Akman et al., 2024) point to advantages in this regard.

In a recent example, (S. Pilz et al., 2024) studied a Ti-42Nb alloy manufactured by L-PBF, followed by heat treatments in the α+β range at about 723 K, with different durations. With increasing treatment time, the precipitation of a metastable orthorhombic phase (α_{iso}'') was observed, which serves as an intermediate step to the stable α phase. These authors also show that the initial precipitation of α_{iso}'' occurs preferentially at the boundaries of β grains, while nucleation is delayed inside the grains. With long treatments, the volume fraction of α_{iso}'' approaches ~25 %. This has a direct impact on the stiffness of the material: the elastic modulus increases as more α_{iso}'' and α appear. The as-built state of L-PBF of Ti-Nb alloys already produced β microstructures with some residual stresses and elongated columnar grains, showing crystallographic texture and, sometimes, micro-defects (small porosity, micro-inclusions (S. Pilz et al., 2024). Moreover, the authors investigated the effect of heat treatment in the mechanical properties of the Ti-42Nb alloy. The results showed that with increased treatment time, in addition to the development of α_{iso}'', there is a significant increase in hardness and strength (yield strength and ultimate tensile strength) compared to the as-built state. For example, after 108 ks, the yield strength reached 1060 MPa, an increase of 50 % compared to the initial state. However, this increase in strength is accompanied by an increase in the elastic modulus, in the case of the same study, up to 87 GPa which can mitigate the advantage of low stiffness typical of β alloys. Therefore, there is a trade-off: post-treatment can improve strength but increase stiffness and it needs to be optimized according to the application (e.g. parts that require higher strength or lower Young modulus as close as possible to the bones').

Previous works have reported the microstructure of a beta Ti-35Nb-7Zr-5Ta (TNZT) biocompatible alloy produced by L-PBF (R. L. Batalha et al. 2022). The melt pools are observed in the image of Figure 2.6a, whereas a closer look shows the solidification structure in Figure 2.6b and 2.6c. It is reported that such structures are observed in additive manufacturing of metals because of the high cooling rates and thermal gradients involved in the L-PBF process (Dwivedi, 2025; Terrazas-Najera et al., 2021;Herzog et al., 2016).

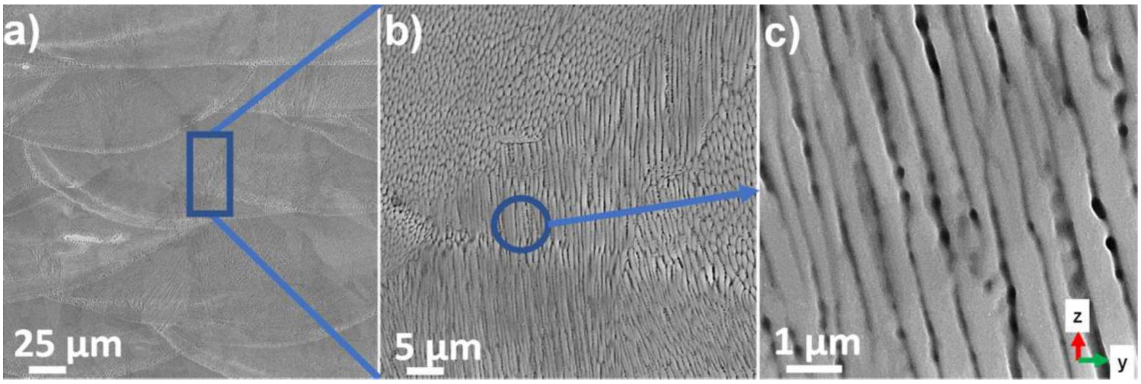

Figure 2.6 - SEM images of TNZT alloy produced by L-PBF (R L Batalha et al., 2022).

In addition to the classic L-PBF process parameters (laser power, speed, hatch spacing, layer thickness), the scanning strategy (scanning direction, rotation between layers, chessboard pattern, etc.) has a strong influence on texture, grain growth and pore distribution. (W. C. Batalha et al., 2023b) compared three scanning strategies (Figure 2.7): unidirectional-Y, bidirectional with 79° rotation between layers (R79), and chessboard (CHB). They observed that R79 and CHB scanning strategies produced very high relative densities (> 99%) and more homogeneous pore distribution, while unidirectional-Y scanning strategy tends to form pores aligned along the scanning direction. Crystallographic texture in material produced with unidirectional-Y presented a strong fiber texture (Figure 2.7c), while R79 showed a weaker texture (Figure 2.7a), CHB more random orientation and equiaxial grains. Mechanical properties were tested, and the lowest Young's modulus was measured for unidirectional-Y, while R79 showed higher yield strength due to lower porosity. These differences show that the scanning strategy is an adjustable fundamental parameter for tuning the microstructure-property relationship.

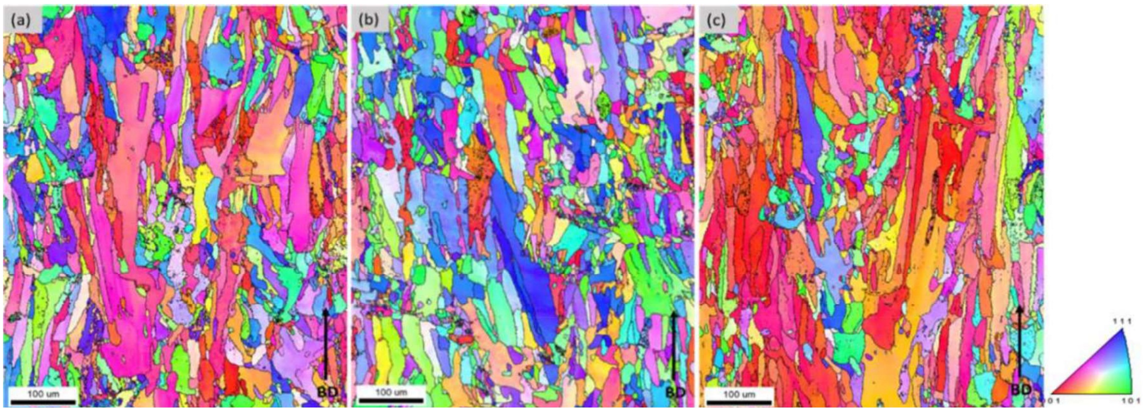

Figure 2.7 - Microstructure of Ti-35Nb-7Zr-5Ta alloy produced by L-PBF with different scanning patterns: a) R79° rotation, b) chessboard, and c) unidirectional-Y. (Adapted from W. C. Batalha et al., 2023).

Therefore, the scanning strategy has a direct impact on the microstructure of the alloys during L-PBF processing, specifically on the orientation and size of the grains, as reported by (W. C. Batalha et al., 2023). Thus, the variation in scanning patterns alters the mechanical properties of the alloy, with configurations that can promote higher microstructure homogenization and improve the strength and stability of the β phase.

Although the Ti-Nb alloys haves showed significant potential, production via L-PBF still faces challenges. Precise configuration of the scanning parameters is essential to control the microstructure and achieve optimal mechanical properties. The literature suggests that advances in 3D printing techniques and the optimization of process parameters are key to expanding the alloy's applications in complex biomedical devices (Tardelli et al., 2024a).

2.5 Porous structures for implants

Bulk structures consist of solid materials with a high level of density that aim to guarantee a high level of robustness. When approached in terms of β-phase Ti-Nb alloys, due to their strength and adequate mechanical properties. When properties such as strength, Young’s modulus and the effect of the loads applied to the body are of interest, bulk cylinders are an appropriate starting reference (Nadammal et al., 2022).

On the other hand, porous structures and scaffolds consist of materials that are manufactured with empty spaces distributed throughout their solid matrix, so that it is possible to obtain a network of interconnected pores (Y. Ma et al., 2024). Scaffolds are three-dimensional porous structures which normally support cell proliferation and tissue regeneration by serving as a base and support (Rehman et al., 2023). The pores can have variable distributions, shapes and sizes depending on the purpose of the application. Recent advances of these types of structures were enabled by additive manufacturing technologies in the field of medical implants, which makes them an important area of research (Aydin et al., 2025; R L Batalha et al., 2022; Rehman et al., 2023; D. Wang et al., 2022).

In the present work, porous cylinders are used to simulate and analyze the behavior of materials with properties like those of cortical bone. Their shape makes them excellent for compression tests, due to the uniform distribution of the applied load, and they can even simulate what bone implants face in the human body as can be seen in Figure 2.8 (L.-C. Zhang et al., 2023). These structures can be designed for additive manufacturing (AM) to mimic the characteristics of bone (with the cortical bone as a reference), focusing above all on reducing weight, obtaining a modulus of elasticity closer to that of bone, improving bone integration, implant fixation and biocompatibility (Y. Ma et al., 2024). Therefore, porous structures are indispensable for obtaining these characteristics, since they allow to reduce stress shielding avoiding implant loosening. Biologically, the significant increase in the area to volume ratio means that the cells have more surfaces to adhere to, producing faster and more effective colonization. It also facilitates the transport of nutrients that are essential for cell proliferation, thus accelerating the formation of specific cells, such as osteoblasts (L.-C. Zhang et al., 2023).

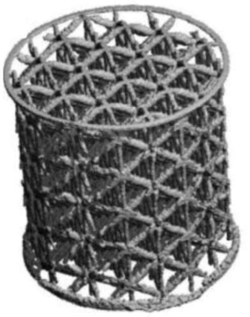

Figure 2.8 - Model of porous cylindrical structures (Rehman et al., 2023).

Currently, there are three different types of porosity that stand out in the biomedical field: Voronoi, diamond and gyroid (Figure 2.9). Voronoi consists of the decomposition of a given space into convex polygons, which do not have a defined pattern and end up being different from each other. It is the porous structure developed to date that is closest to that of human trabecular bone and has good bone integration. Diamond consists of a regular structure made up of interconnected nodes that provide uniform load distribution. Due to its shape, it has high structural strength and uniform rigidity (great for supporting high loads). Finally, gyroid consists of continuous geometry with no intersections, which is widely used when good strength is required. Due to its continuous geometry, gyroid structures play an excellent role in the passage of nutrients and in load transfer, while according to studies it manages to obtain Young's modulus values close to those of cortical bone, making this porous structure very promising (Tyagi & M, 2023).

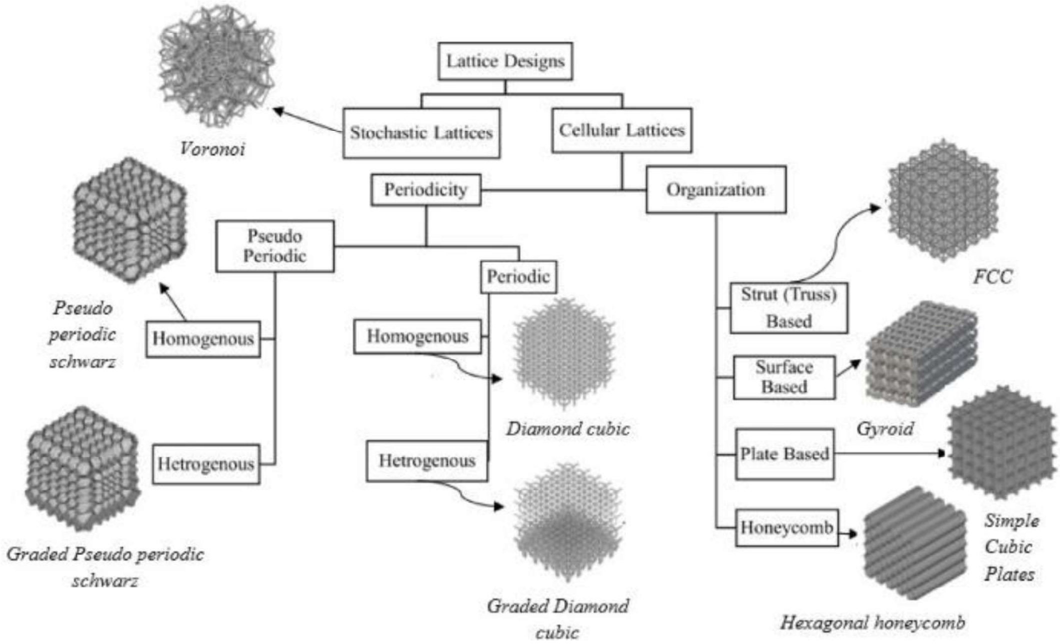

Figure 2.9 - Classification of lattice structures based on geometrical distribution (Tyagi & M, 2023).

When manufacturing structures make use of additive manufacturing technologies such as L-PBF, the design space is significantly enlarged, allowing new geometries to be produced. In the case of bulk structures, the aim is to achieve a relative density of 100%, so that the strength and homogeneity of the structure are optimized as much as possible. For this to be possible, it is necessary to select an appropriate value of laser power, scanning speed and a hatching distance. These parameters ensure complete melting of the powder particles and minimize unwanted porosity in the material (Nandhakumar & Venkatesan, 2023). Therefore, bulk geometries are usually produced in the form of standardized specimens, which are used for mechanical tests such as tensile and compressive for characterizing the mechanical properties of materials. When manufactured, they must follow the requirements of standards such as the ISO/ASTM 52909, which address and specify the methods for tensile, compressive and fatigue tests (respectively) for metallic materials and guidelines on their geometry (T. Deng et al., 2025; Liu et al., 2023; Tardelli et al., 2024b).

While bulk structures are used to optimize the L-PBF parameters and test the bulk properties of materials, with porous structures, the aim is to be able to control the built of lattice structures without compromising the strength of the structure. To this end, the laser must be adjusted specifically for the porous geometry to achieve highest precision in terms of pore size, morphology and distribution (Pan et al., 2020; Tyagi & M, 2023; Yu et al., 2022). Hence, the L-PBF technology makes it possible to create a controlled porous structure in Ti alloys, as can be seen in Figure 2.10. For medical implants, the porosity is important for promoting bone integration, allowing bone to grow inside the implant. Furthermore, the modulus of elasticity of the implant can be tuned by adjusting the porosity, mimicking the bone structure and thus reducing the risk of stress shielding (Pesode & Barve, 2023).

Figure 2.10 - Implants of titanium with controllable structural units fabricated by laser powder bed fusion (L.-C. Zhang et al., 2023).

Chapter 3

Materials and Methods

This chapter provides a comprehensive overview of the experimental methodologies employed in this study, encompassing both the manufacturing process and the subsequent characterization techniques used to evaluate the produced alloys. These include, microstructure characterization (optical and scanning electron microscopy), as well as chemical composition analysis (spark emission spectroscopy and carrier gas heat extraction technique), and mechanical tests (tensile and compression). Together, these methods enable a holistic evaluation of the alloys in terms of mechanical performance, structural integrity, phase constitution, and chemical homogeneity, which are critical parameters for their intended application in biomedical devices.

3.1. Feedstock powder materials

The materials used in this study are commercially pure Ti Grade 2 (m4p GmbH) and Ti-6Al-4V ELI Grade 23 (m4p GmbH). Pure Ti Grade 2 and Ti-6Al-4V ELI Grade 23 were supplied as powders produced via argon gas atomization with spherical particles, particle size of 15-45 μm and chemical composition corresponding to the medical grades specified in the ASTM F67-24 and the ASTM F1472-23 Standards. The AMPERIT pure Nb (99.5% purity, Flame Spray Technologies BV) used to prepare the Ti-Nb alloy was supplied as fused and crushed non-spherical powder with particle size 5-45 μm. The Ti-39Nb powder mixture was then obtained by mixing the pure Ti and pure Nb using a drum hoop mixer (JEL RRM Mini-II, J. Engelsmann AG) for 5 hours at a speed of 35 rpm, and 2.35 kg of Ti-39Nb powder mixture was prepared (Lisboa Batalha, 2019).

The powders were characterized by measuring particle size distribution (PSD) and particle morphology, according to ASTM F3509-25, with the following techniques and respective instruments: Dynamic Image Analysis (DIA) for PSD and particle morphology with the CamSizer X2 instrument (MICROTRAC MRB). The technique used was dry, pressurized air dispersion. Three measurements were performed for each sample. Particle morphology and surface texture were further observed in a Scanning Electron Microscope (SEM, Hitachi SU3900), with secondary electrons (SE) and back-scattering electrons (BSE) detectors. Local chemical analysis of the powers was performed using energy-dispersive spectroscopy (EDS, Bruker XFlash 730M).

3.2. Methodology

3.2.1. Computational design of geometries

The design of the bulk test specimens was carried out using Autodesk Fusion 360 software, which enabled precise modeling of the geometries to be produced via additive manufacturing. Two primary specimen types were developed: cylindrical samples with a diameter of 10 mm and a height of 30 mm, intended for compression tests, and cubic samples with dimensions of 10 × 10 × 10 mm, designed to assess microstructure and density, as can be seen in Figure 3.1. Moreover, bulk cylinders with ϕ 12 mm x 50 mm height were modelled for machining specimens for tensile tests. These geometries were selected based on their relevance to mechanical characterization and their suitability for assessing bulk properties of the Ti-based materials used in this work.

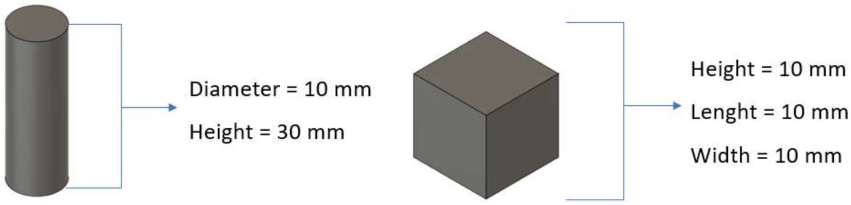

Figure 3.1 - Geometries of cylindrical and cubic samples.

The computational modeling of the porous structures was carried out using the nTop software (version 5.15.2), which allowed the design of six distinct configurations for both the scaffold and cylindrical specimen groups. The structures were developed with controlled porosity levels and unit cell dimensions. The configurations were selected to evaluate the influence of pore morphology and distribution on the mechanical and biological performance of the Ti-based alloys fabricated by L-PBF. The control over porosity and unit cell dimensions is crucial for tailoring the elastic modulus and enhancing cell integration in biomedical implant applications as others mechanical properties, like yield strength.

Therefore, cylindrical scaffolds with gyroid and Voronoi porous architecture were implemented. Each of them was generated at three different porosity levels 50%, 65%, and 75%. The corresponding unit cell size and point spacing are presented in Table 3.1 and the modelled porous geometries are shown in Figure 3.2.

3.2.2. Prototyping

Before producing the porous structure of the Ti-based alloys by laser powder bed fusion (L-PBF), prototyping of the geometries was performed, following two main approaches: 3D printing by Material Extrusion with polylactic acid (PLA) and Stereolithography (SLA) with resin (Formlabs white resin V5). Those 3D printing technologies were chosen for specific evaluation criteria from mechanical handling to visual and morphological inspection. The prototypes served as physical references to test the viability of the complex porous structures and to adjust the 3D models before producing the final titanium-based samples.

Table 3.1 – Design parameters of the six different lattice structures.

Structure	Cell Size (mm)	Pore Size	Beam Thickness (μm)	Point Spacing
Gyroid 50%	0.90	--	80	100
Gyroid 65%	1.20	--	80	100
Gyroid 75%	1.60	--	80	100

Voronoi 50%	0.60	--	80	100
Voronoi 65%	0.76	--	80	100
Voronoi 75%	0.90	--	80	100

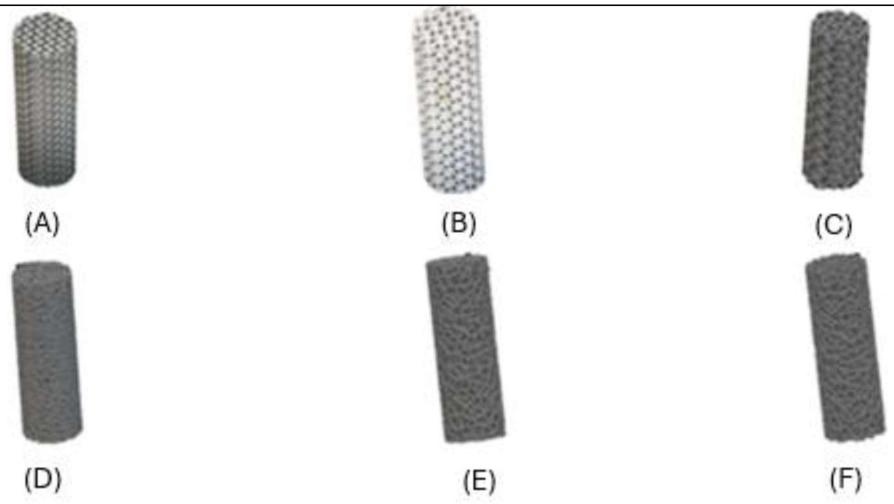

Figure 3.2 - Modelled cylinders with (A) gyroid, 50% porosity and unit cell size of 0.9 mm, (B) gyroid, 65% porosity and unit cell size of 1.2 mm, (C) gyroid, 75% porosity and unit cell size of 1.6 mm, (D) Voronoi, 50% porosity and unit cell size of 0.6 mm, (E) Voronoi , 65% porosity and unit cell size of 0.76 mm, (F) Voronoi, 75% porosity and unit cell size of 0.9 mm.

Material Extrusion of PLA filament with 1.75 mm was employed as a preliminary step in the validation of the designed porous geometries, taking advantage of one of the lowest cost accessible and widely used methods in Additive Manufacturing. The Raise3D Pro2 Plus PLA printer was used, which worked with a 0.4 mm diameter nozzle at 215°C and the platform heated to 55°C.

Stereolithography with resin was employed as a complementary method to Material Extrusion, aiming to overcome some of the limitations encountered in the earlier stages, particularly in terms of resolution and surface detail. The FORMLAB 3+ SLA printer was used, which created the structure through the curing process of the resin (Rigid White) in layers of 0.02 mm by 0.02 mm. It provided enhanced precision and conformity, which are crucial for accurately replicating complex porous architectures, especially those based on Voronoi geometry.

3.2.3. Samples fabrication by Laser Powder Bed Fusion

The fabrication of the Ti-based samples was carried out using the laser powder bed fusion (L-PBF), employing process parameters optimized by Renishaw for Ti alloys (Renishaw plc), which are widely validated in both industrial and academic. This ensured the reproducibility and reliability of the manufacturing process across the different material systems studied, namely pure Ti, Ti-6Al-4V, and Ti-39Nb.

Therefore, the samples were produced by (L-PBF) in a Renishaw RenAM 500S Flex system equipped with a 500 W ytterbium fiber laser (λ = 1080 nm) operating in continuous mode, with a laser spot size of 80 µm. A reduced build volume of 78 × 78 × 50 mm³ was employed, requiring significantly less powder material while maintaining process stability. The samples were fabricated on pure Ti (Grade 2) build plates (W: 78 mm, L: 78 mm, t: 9 mm) at room temperature, with a laser focus position F = 0 mm, and meander 67° rotation scanning strategy. To maintain an inert environment, a continuous flow of high-purity argon gas (99.999%) at 190 m^3/h was applied, keeping the oxygen concentration inside the chamber consistently below 1000 ppm. Figure 3.3 shows the L-PBF process of a batch of cylinders with porous structure.

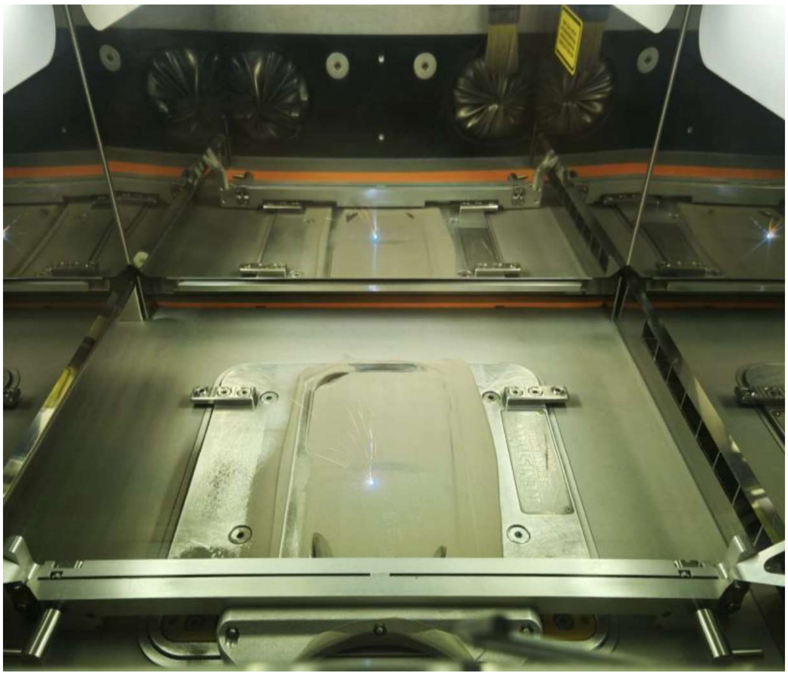

Figure 3.3 - Cylinders with porous structure being produced by L-PBF.

The final parameters used to produce the bulk and porous geometries are presented in Table 3.2. In the end, a total of 75 samples were produced: 54 with porous structures (18 for each type of material with the structures of Table 3.1), 18 bulk cylinders for each type of material (compression test and tensile test in both building and scanning directions), and 3 cuboids (one of each material). After fabrication, all samples underwent a standardized post-processing sequence consisting of sectioning, ultrasonic cleaning (Ultrawave IND Series), and compressed air drying, followed by density and porosity evaluation via Archimedes' principle to confirm conformity with the 3D modelled geometries.

Table 3.2. - Parameters of the L-PBF process used to produce the bulk and porous geometries of the Ti-based alloys.

Samples	Hatch laser power (W)	Scanning speed (m/s)	Hatch distance (mm)	Beam compensation (mm)	Single scan laser power (W)	Layer thickness (mm)
Pure Ti - bulk	280	0.95	0.10	0.095	--	0.03
Pure Ti -	280	0.95	0.10	0.095	85	0.03

porous						
Ti-6Al-4V - bulk	280	0.95	0.10	0.095	--	0.03
Ti-6Al-4V - porous	280	0.95	0.10	0.095	85	0.03
Ti-39Nb - bulk	280	0.95	0.10	0.095	--	0.04
Ti-39Nb - porous	280	1.00	0.09	0.095	85	0.04

During the initial manufacturing stage, the first batch of samples was fabricated to evaluate the influence of specific process parameters on the final part quality (Figure 3.4). At this stage, a set of samples was produced with the standard parameters, while other set was fabricated with the addition of downskin parameters and a third set was produced with beam compensation of 0.095 mm. This strategy allowed a comparative assessment of the effects of these adjustments on porosity levels, dimensional accuracy, and the integrity of under-supported surfaces. The results presented in Chapter 4 **–** Results and Discussion refer to samples of optimized quality.

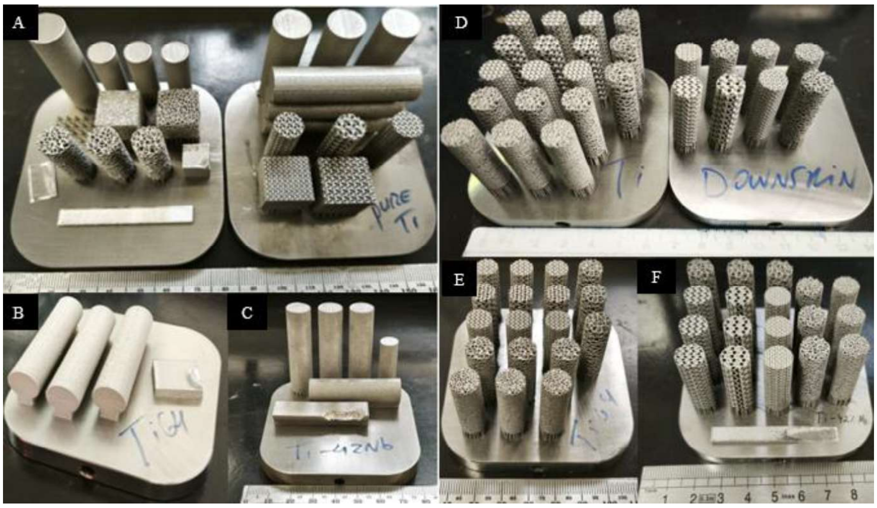

Figure 3.4 - Bulk and porous samples manufactured in L-PBF of (A) pure Ti alloys, (B) Bulk samples of Ti-6Al-4V alloys, (C) Bulk samples of Ti-39Nb alloys, (D) pure Ti scaffolds with (left) and without downskin (right), (E) Ti-6Al-4V scaffolds, and (F) Ti-39Nb scaffolds.

3.2.4. Calculation of porosity

To verify whether the actual produced structures presented the theoretical porosity designed in the CAD models, two different methods were employed to estimate the porosity of the samples. In the first one, mass (m) and volume (v) of each specimen were carefully measured with a Kern ACS digital scale and digital caliper, respectively. The density (ρ) of each sample was calculated using the equation $\rho = \frac{m}{v}$. Subsequently, the porosity percentage (P%) was determined by comparing the densities of the bulk and porous samples using the following equation: $P\% = (1 - (\frac{\rho\ porous}{\rho\ bulk})*100)$.

The second method to calculate the porosity consisted of measuring *m* and *v* of the porous samples. Then, the known density of the materials was obtained from their respective datasheets. This enabled a more material-specific analysis, where porosity was calculated as $P\% = (1 - \frac{m}{V*\rho})*100$, with ρ as theoretical density of the material in its fully solid (non-porous) state.

3.2.5. Materials characterization

The bulk chemical composition of the alloys was obtained by spark emission spectroscopy using the OBLF QSN 750II spectrometer (Gesellschaft für Elektronik und Feinwerktechnik GmbH). The carrier gas heat extraction technique (CGHE; LECO) was applied to analyze the oxygen, nitrogen and oxygen content of the Ti-based alloys. At least three analyses for each element were performed.

Structural analysis was performed in the investigated materials to investigate the phases with powder X-ray diffraction in a Rigaku MiniFlex diffractometer, using a Cu kα (λ = 1.5406 Å) radiation operated at 30 kV and 15 mA in Bragg-Brentano geometry. The scan range used was 20-90° with a step size of 0.02º and scan speed 0.5º/min. Moreover, microstructural observations were performed on samples of powder, bulk and porous structures of pure Ti, Ti-6Al-4V, and Ti-39Nb. For the bulk samples, cross-sections were cut from both the cuboid and the tensile specimen of each material, enabling the evaluation of the microstructure along the scanning direction (SD) and building direction (BD). Then, metallographic samples were prepared as follows: Firstly, the samples were hot mounted in a conductive phenolic resin (BUEHLER PhenoCure™) using the SimpliMet™ 4000 mounting system by BUEHLER. Then, the samples were subjected to a grinding process, using abrasive SiC papers in a BUEHLER EcoMet 30 polishing machine in the following sequence: 320p, 400p, 600p, 800p, 1000p, 1250p, 2500p, and 4000p. Between each grit size, the sample was rotated 90° to promote uniform surface finishing. A final polishing step was performed with colloidal silica polishing slurry (BUEHLER MasterMet™ Colloidal Silica with 0.06 µm particle size), using detergent as lubricant. The polishing process was carried out 7-10 minutes, followed by a final 1 minute of polishing under running water. The polished samples with mirror-like surfaces are shown in Figure 3.5.

Figure 3.5 - Metallographic samples after polishing.

The metallographic samples prepared were then observed with a Nikon Eclipse LV150N optical microscope (OM), with an integrated Imaging Source 5 MP digital camera (Figure 3.6a). The magnifications used were 50x, 100x, 200x, 500x, and 1000x. The polished samples were first observed to evaluate internal quality. To further reveal the microstructure, the samples were etched with Kroll's reagent for 20 seconds. Then, the micrographs were obtained using the same OM. Furthermore, the microstructure of the Ti alloys was observed in the Hitachi SU3900 Scanning Electron Microscope (Figure 3.6b), using the secondary electrons (SE) and back-scattered electrons (BSE) detectors. Local semi-quantitative analysis was performed with an energy-dispersive spectroscopy (EDS, Bruker XFlash 730M) detector in the SEM.

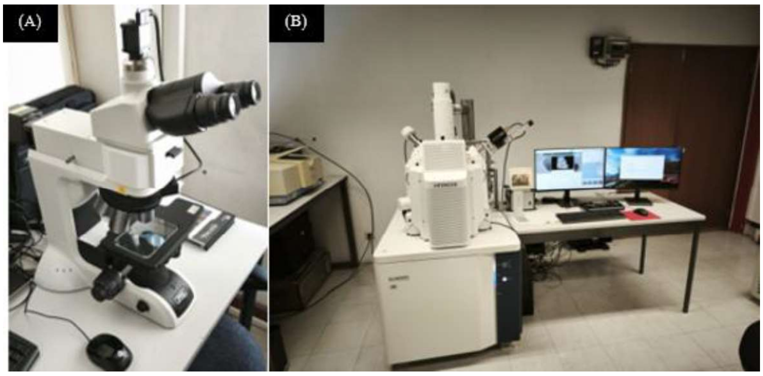

Figure 3.6 – (A) Optical microscope Nikon Eclipse Vision, (B) Scanning electron microscope Hitachi SU3900.

3.2.6. Mechanical tests

In the present study, two mechanical tests were conducted: tensile and compression tests. The tensile test was employed to evaluate properties such as ultimate tensile strength, yield strength, and elongation at fracture, thereby characterizing the material's response under uniaxial tension. Conversely, the compression test was performed to assess the material's behavior under compressive loading, providing complementary data on its strength and stability when subjected to forces that induce shortening rather than elongation. Together, these tests allowed for a comprehensive mechanical characterization of the materials and geometries.

3.2.7. Tensile tests

Tensile testing is one of the most employed mechanical characterization techniques due to its relative simplicity of execution, high reproducibility and the breadth of information it provides regarding the behavior of materials under uniaxial loading. From a single test, it is possible to determine key mechanical properties such as ultimate tensile strength (UTS), yield strength (upper and lower, depending on the material), elastic modulus, uniform and total elongation and reduction of area. These parameters are fundamental in the selection, comparison, and qualification of materials for engineering applications, where mechanical performance under static loading is a critical design criterion.

Tensile tests are generally performed at room temperature under controlled laboratory conditions, unless otherwise specified for elevated-temperature or environmental studies. The geometry and dimensions of the specimens must conform to the relevant standards to ensure comparability of results.

In the European context, the most used specifications are provided by ASTM E8/E8M-22 (ASTM international, 2022), where proportional and non-proportional specimens are defined with precise tolerances regarding gauge length, width, thickness, and transition radii.

For the execution of the test, the standardized specimen is mounted in the grips of a universal testing machine (UTM), ensuring proper alignment to avoid bending stresses. An extensometer is typically attached to the gauge length of the specimen to measure strain with high accuracy during the elastic and early plastic regime (Figure 3.7a). The tensile test was performed on specimens machined out of cylinders produced with vertical (building direction) and horizontal (scanning direction) orientations (Figure 3.7b). The test proceeds by applying a tensile load in the axial direction under displacement or strain control, generally at a constant crosshead speed or according to a prescribed strain rate until the specimen fractures.

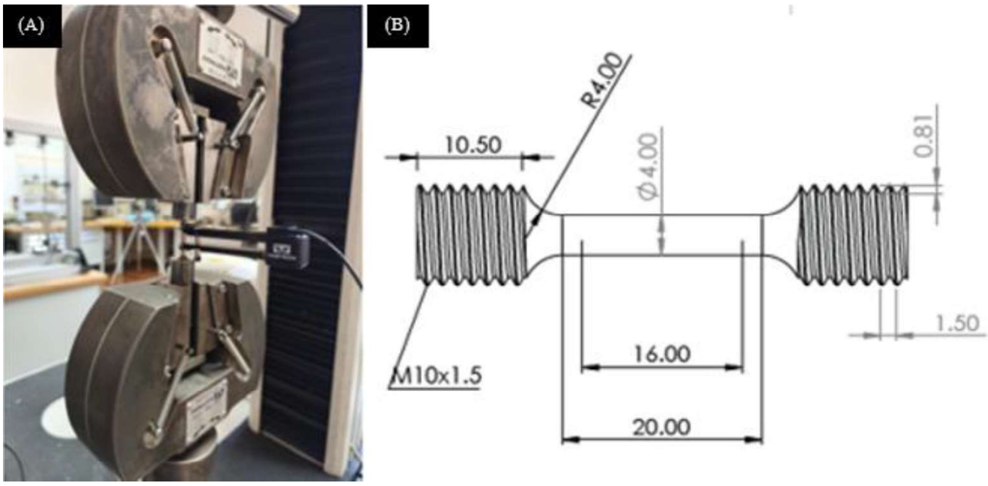

Figure 3.7 – (A) Tensile testing on Instron 3369 universal testing machine and (B) machined cylindrical specimens of the Ti alloys. measures

During the test, the machine continuously records the applied load and the corresponding elongation, producing a stress strain curve (engineering stress vs. engineering strain). This curve provides insight into the elastic region (from which the Young’s modulus and yield strength can be determined), the plastic region (characterized by strain hardening and culminating at the UTS), and the fracture point. Depending on the ductility of the material, the curve may exhibit distinct upper and lower yield points, a plateau region, or necking phenomena prior to failure.

The results are typically reported as the mean value and standard deviation of several replicate tests, ensuring statistical reliability. Furthermore, post-test fractography (optical microscopy or SEM) can provide complementary information about the failure mechanism (ductile, brittle, or mixed).

The tensile tests were conducted at Instituto Superior Técnico (IST), within the Department of Mechanical Engineering, following standardized procedures in accordance with ASTM E8/E8M-22 for metallic materials. All experiments were performed using an Instron 3369 universal testing machine equipped with a 50 kN load cell to ensure accurate force measurements, and a 12.5 mm extensometer for precise strain acquisition within the gauge section, as can be seen in Figure 3.7. The tests were performed on machined specimens.

The machine was programmed with a crosshead displacement rate of 2 mm/min, a parameter chosen in compliance with the ASTM standard and to minimize dynamic effects, thereby ensuring quasi-static loading conditions. All tests were carried out at an ambient temperature of approximately 24°C under laboratory-controlled conditions to guarantee consistency and eliminate the influence of thermal fluctuations on the material response.

The testing sequence was organized to first evaluate vertically and horizontally built bulk specimens of pure Ti. Subsequently, tensile tests were performed on Ti-6Al-4V specimens, followed by Ti-39Nb specimens. This systematic approach enabled a comparative analysis of the influence of alloy composition and manufacturing orientation on the tensile properties, providing a comprehensive understanding of the mechanical performance of the materials investigated under standardized testing conditions.

After the acquisition of experimental data, a systematic data processing procedure was carried out. For the tensile tests, different approaches were employed depending on the elastic behavior of the materials. In the case of materials exhibiting a predominantly linear elastic response, namely pure Ti and Ti-6Al-4V, the data were processed using Microsoft Excel. Conversely, for Ti-39Nb, which demonstrated a nonlinear elastic response, the analysis required a combined approach using Microsoft Excel along with a custom developed Python script to ensure accurate determination of mechanical properties.

For pure Ti and Ti-6Al-4V ELI, the 0.2% offset method was applied in accordance with standard procedures to determine the yield strength. This method consists of constructing a line parallel to the initial linear portion of the stress–strain curve, offset by a strain of 0.002 (0.2%), and identifying its intersection with the experimental curve. The modulus of elasticity (Young's modulus) was obtained from the slope of the elastic region.

For the Ti-39Nb alloy, due to its nonlinear elastic behavior, the traditional offset method was not applicable. Instead, a combination of tangent and secant methods was implemented. The tangent method was used to estimate the initial elastic slope, while the secant method provided a more accurate representation of the material's stiffness over the relevant strain range. These techniques allowed for the precise calculation of Young's modulus and yield strength for this alloy, despite its unique anelasticity characteristics.

3.2.8. Compression tests

Compression testing is a fundamental mechanical characterization technique used to evaluate the behavior of materials subjected to uniaxial compressive loading. It allows the determination of key properties such as the compressive strength, the elastic modulus, the limits of elastic and plastic deformation, and in some cases, phenomena such as buckling, barreling, or failure modes associated with instability. These parameters are essential for applications where materials are primarily subjected to compressive stress, such as structural supports, biomedical implants, or energy absorption components.

The tests are carried out at room temperature under controlled laboratory conditions, unless specific environmental conditions are required. The geometry and dimensions of the specimens must comply with international standards to guarantee reproducibility and comparability of results. In most cases, cylindrical specimens (height-to-diameter ratio between 1.5:1 and 2:1) or rectangular prisms are used, with surface flatness and parallelism being critical to ensure uniform stress distribution during loading. Standards such as ASTM E9 (Test Methods of Compression Testing of Metallic Materials at Room Temperature, 2025) provide detailed requirements regarding specimen preparation, alignment, and test procedures.

For the execution of the test, the specimen is carefully positioned between parallel platens, ensuring proper alignment to minimize bending stresses. A compressive load is then applied in the axial direction under displacement control or strain-rate control, typically at a constant crosshead speed corresponding to a prescribed strain rate. The test proceeds until a defined strain level, a maximum load, or until failure occurs, depending on the objective of the study.

Throughout the test, the machine continuously records the applied load and the corresponding displacement, generating a compressive stress - strain curve. This curve enables the identification of the elastic regime (from which the compressive modulus is determined), the onset of plastic deformation, the yield point (if present), and the maximum compressive strength. Depending on the material, the curve may also reveal nonlinear behavior such as strain hardening, densification (in porous materials), or sudden fracture.

To ensure statistical validity, multiple specimens were tested under identical conditions, and the results are reported as mean values with standard deviation.

The compression tests of the porous cylinders (showed in Figures 3.2 and 3.4) were conducted at IST/Department of Mechanical Engineering, following standardized procedures in accordance with EN E9 for metallic materials. Porous specimens were performed using an Instron 3369 universal compressive testing machine, with a 50 kN load capacity and a displacement rate range of 0.005–500 mm/min, as can be seen in Figure 3.8. The machine's high precision load cell and servo motor system ensure accurate force and displacement measurements. Each measuring 10 mm in height was compressed at a constant displacement rate of 2 mm/min until reaching 33% deformation (total displacement of 10 mm). Nine specimens per lattice structure type are tested (3 for each material), with compression applied along the build direction to assess compressive mechanical performance. The tests were carried out at an ambient temperature of approximately 24 °C under laboratory-controlled conditions to guarantee consistency and eliminate the influence of thermal fluctuations on the material response. For bulk specimens (cylinders ϕ10 x 30 mm showed in Figure 3.1 and 3.4), an Instron hydraulic compression testing machine with a 100 kN load cell was used. The crosshead displacement was maintained at 2 mm/min, and the room temperature was also 24 °C. The test was performed until the final length of the cylinders was 10 mm, with a constant displacement rate of 2 mm/min until reaching 33% of deformation. A total of 10 bulk specimens were tested (3 of pure Ti, 3 of Ti64 and 4 of Ti-39Nb).

Figure 3.8 - Compression test of a cylinder with gyroid structure on the Instron 3369 universal testing machine.

3.2.9. Fractography of the mechanical tested specimens

Following the completion of the mechanical tests, the fracture surface of a representative tensile specimen for the tested materials in the vertical (building direction) and horizontal (scanning direction) orientations from each of the investigated materials were selected for fractographic examination. The specimens were first observed directly in the scanning electron microscope (Figure 3.9 (A) and (B)). The mounted samples were initially analyzed using optical microscopy to observe the general microstructural features and to identify the fracture plane morphology. Subsequently, a more detailed analysis was performed using a SEM to examine the fracture surfaces at higher magnifications. This approach allowed for the assessment of fracture characteristics, the propagation path of cracks, and the dominant failure mechanisms. Special attention was given to identifying the presence of ductile fracture features, particularly the classic cup and cone morphology, which is typically associated with materials exhibiting significant plastic deformation prior to failure. These observations provided critical insights into the fractured behavior of the tested alloys and their relationship to microstructural characteristics induced by composition and processing conditions.

Furthermore, the porous cylinders were observed after performing mechanical compression tests using the SEM to establish the correlation between the recorded mechanical behavior and the associated failure mechanisms. The analysis focused on characterizing the fracture mode and position of the fracture initiation in the porous geometries and the possible occurrence of pore crushing or alignment, phenomena that are particularly relevant in such structures.

Figure 3.9 – Fractured tensile specimens: (A) horizontal build and (B) vertical build.

Chapter 4

Results and discussion

This chapter presents the results obtained in the characterization of the powders, manufactured bulk and porous structures and mechanical tests. The discussion is carried out in parallel with literature, to better critical compare and frame the results with state of the art.

4.1. Powder characteristics

The particle size distribution (PSD) of the pure Ti Grade 2, Ti-6Al-4V ELI and pure Nb powders is presented in Figures 4.1-part A, 4.2- part A and 4.3- part A. It can be noted that Pure Ti particles ranged from approximately 25 µm (d10) to 44 µm (d90), with a median size (d50) of 34 µm, as shown in the figure 4.1-part A. In the case of Ti-6Al-4V ELI Grade 23 x15, the distribution extended from 27 µm (d10) to 48 µm (d90), with d50 = 35 µm and an average particle size of 35 µm, as shown in the figure 4.2-part A. Finally, the Ti-Nb alloy presented a distribution ranging from 19 µm (d10) to 47 µm (d90), with a median size (d50) of 33 µm and an average particle size of 33 µm, as shown the figure 4.3-part A. The particle size distributions of all three powders are within the standard particle size distribution commonly used for laser powder bed fusion (Penny et al., 2025; L. C. Zhang et al., 2023)

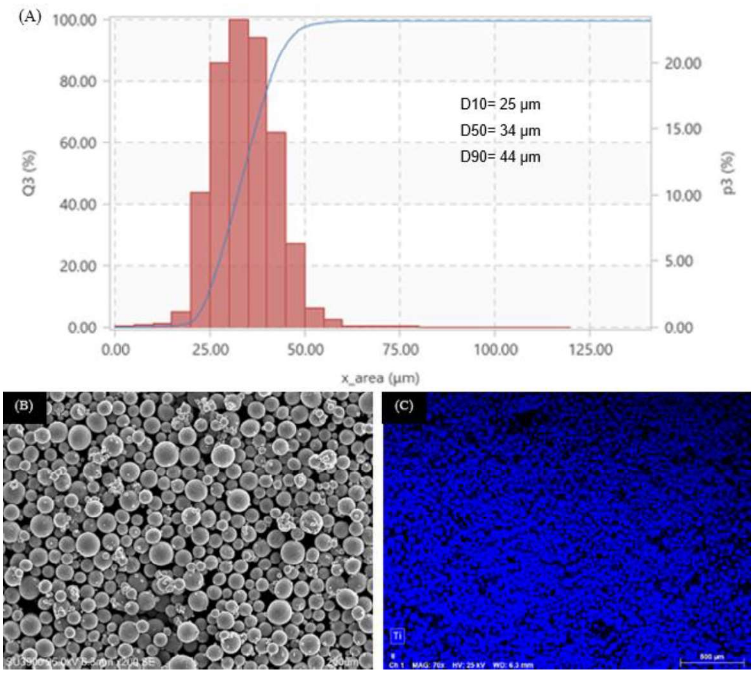

Figure 4.1 – Pure Ti powder: (A) particle area distribution and cumulative frequency, (B) Powder morphology with SEM image of Gas atomized Pure Ti powder and (C) EDS map.

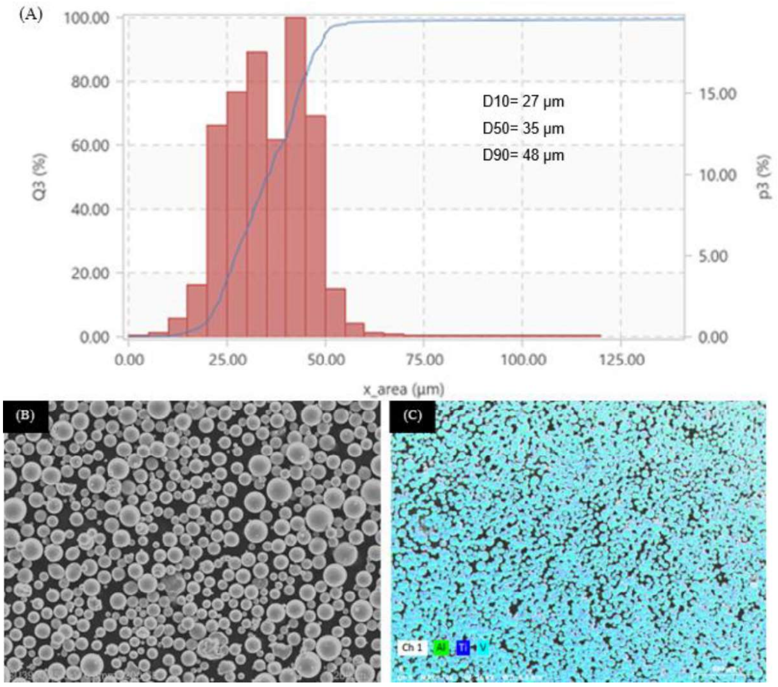

Figure 4.2 – Ti-6Al-4V powder: (A) particle area distribution and cumulative frequency, (B) Powder morphology with SEM image of Gas atomized Ti-6Al-4V powder and (C) EDS map.

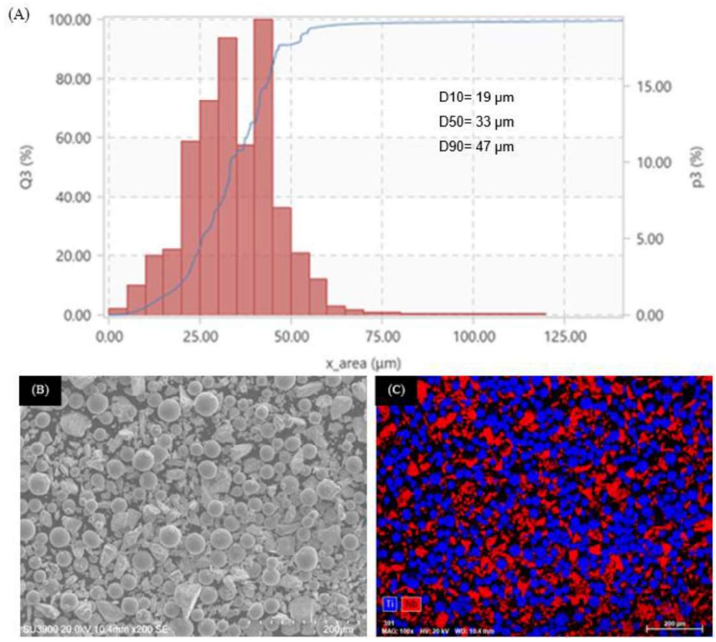

Figure 4.3 – Ti-39Nb powder: (A) particle area distribution and cumulative frequency, (B) Powder morphology with SEM image of Ti-39Nb powder mix and (C) EDS map.

The morphological analysis of the powders carried out by SEM revealed clear differences between the materials studied. The particles of pure Ti (Figure 4.1- part B and C) and Ti-6Al-4V (Figure 4.2- part B and C) exhibit a predominantly spherical morphology, characteristic of powders produced by gas atomization, which favors good flowability, high packing density, and homogeneous melting behavior during the L-PBF process. In contrast, the Ti-39Nb powder mixture presented two distinct morphologies:

Spherical particles corresponding to titanium and irregular polygonal particles corresponding to niobium, as show in Figure 4.3- part B and C. The irregular shape of Nb particles hinders the spreading process, reducing the overall flowability of the powder. Moreover, the non-spherical particles may lead to non-uniform packing and local heterogeneities during laser melting, which could translate into microstructural inhomogeneities in the final bulk material (L. C. Zhang et al., 2023). The corresponding EDS maps further corroborate these findings has been already observed by (Ersoz et al., 2024).

4.2. Bulk chemical analysis

Chemical analysis of the Ti and Ti alloys revealed results compatible with biomedical applications. Pure titanium showed very low levels of oxygen (0.016 wt.%), by infrared absorption and nitrogen (0.010 wt.%), by thermal conductivity, well within the limits of ASTM F67, indicating high purity, while hydrogen (>0.006 wt.%) remains close to the detection limit. For the Ti-6Al-4V alloy, the Al (6.1 wt.%) and V (4.0 wt.%) contents, determined by spark emission spectroscopy, are very close to the nominal composition, in accordance with ASTM F136, and the residual presence of iron (0.16 wt.%) is small. The interstitial elements O (0.012 wt.%) and N (0.004 wt.%), measured by infrared absorption are also low in the Ti-6Al-4V ELI alloy, which are important for minimizing embrittlement effects. The Ti-39Nb alloy has 60.6 wt.% Ti and 39.4 wt.% Nb, by spark emission spectroscopy, with no traces of Al or V, reinforcing the alloy's biocompatibility, while O (0.006 wt.%) and N (0.011 wt.%) remain low. The low standard deviations (σ Ti ≈ 0.09 wt.%; σ Nb ≈ 0.06 wt.%) confirm the reliability of the analysis, as shown in Table 4.1. Overall, all alloys show minimal contamination by interstitial elements, benefiting ductility and mechanical strength, and allowing for a clear comparison of the properties of the alloys studied (Zhuo et al., 2025).

Table 4.1 - Chemical analyses of the Ti alloys (wt.%).

Reference	Ti (%)	Al (%)	V (%)	Fe (%)	Nb (%)	O (%)	N (%)	H (%)
Pure Ti	--	--	--	--	--	0.016	0.010	>0.006
Ti-6Al4V ELI	89.8 ± 0.1	6.1 ± 0.1	4.0 ± 0.03	0.16 ± 0.01	--	0.012	0.004	>0.006
Ti-39Nb	60.6 ± 0.1	--	--	--	39.4 ± 0.06	0.006	0.011	>0.006

4.3. Real porosity of scaffolds

The theoretical porosity of the scaffolds was designed using the nTop - software with 50%, 65% and 75% porosity. On the other hand, the relative density determined by Archimedes' principle showed slight variations from the planned values. In most cases, the deviations observed are small (±3%), demonstrating good manufacturing precision, as shown in Table 4.2.

Tabel 4.2 - Porosity values calculated after measuring the density with Archimedes principle.

Scaffold	Pure Ti	Ti6Al-4V	Ti-39Nb
Cylinder Gyroid 50%	54 ± 3%	54 ± 3%	51 ± 3%
Cylinder Gyroid 65%	67 ± 3%	66 ± 3%	63 ± 3%
Cylinder Gyroid 75%	75 ± 3%	74 ± 3%	72 ± 3%
Cylinder Voronoi 50%	50 ± 3%	50 ± 3%	47 ± 3%
Cylinder Voronoi 65%	64 ± 3%	62 ± 3%	67 ± 3%
Cylinder Voronoi 75%	77 ± 3%	80 ± 3%	85 ± 3%

However, certain scaffolds, namely those manufactured with Ti-39Nb and 75% Voronoi geometry, showed a more pronounced deviation, with actual porosity of approximately 85%, well above the 75% designed. This behavior can be attributed to multiple factors intrinsic to the L-PBF process, including material contraction during solidification, melting imperfections, differences in geometry between gyroid and Voronoi, and process parameters such as laser power, scanning speed, and layer thickness. Furthermore, analysis of the powder morphology (performed previously) revealed that the Nb particles have an irregular, polygonal shape, in contrast to the sphericity observed in the Ti particles, which may contribute to the formation of local voids or incomplete melting, increasing the actual porosity compared to theoretical porosity. Previous studies on L-PBF of Ti64 and Ti-Nb report typical deviations of ± 3 to 5% between designed and calculated porosity, with Voronoi scaffolds generally being more susceptible to variations due to their geometric complexity (Y. Ma et al., 2024). In relation to the 75% Voronoi scaffold made from Ti-6Al-4V (measured porosity of 80%), the deviation may be due to slight contraction of the material in the walls, leading to a higher-than-expected value of porosity or presence of some defects (Figure 4.4). Despite these deviations, the results obtained are considered adequate for biomedical applications, given that the difference between the projected and actual porosity is small, predictable, and compatible with the desired structural functionality.

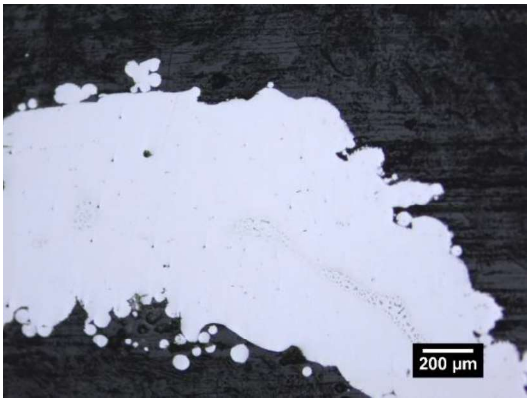

Figure 4.4 – Polished surface of gyroid 75% observed by OM

4.4. Microstructural and crystallographic characterization

Crystallographic characterization was performed by XRD. Figure 4.5 presents the XRD patterns for pure Ti (powder and bulk), Ti-6Al-4V ELI (bulk) and Ti-39Nb (bulk) materials produced by L-PBF. It may be noticed that pure Ti has α/α′ (martensite) crystal structure in the raw material (powder) and as-built (after L-PBF process) (Attar et al., 2014; A. Cheng et al., 2014; Gu et al., 2012). The same crystal structure was also detected in the Ti-6Al-4V ELI alloy α′ (hcp martensite), which is a result of the high cooling rate evolved in the L-PBF process (Simonelli et al., 2014; Vrancken et al., 2012). On the other hand, the high amount of Nb, which is a strong beta-stabilizer in Ti alloys, leads to a β-Ti structure in the Ti-39Nb alloy, which is known for its lower Youngs modulus and, therefore, to induce better biomechanical compatibility (R L Batalha et al., 2022; Rodolfo Lisboa Batalha et al., 2020; S. Pilz et al., 2024; Stefan Pilz et al., 2022).

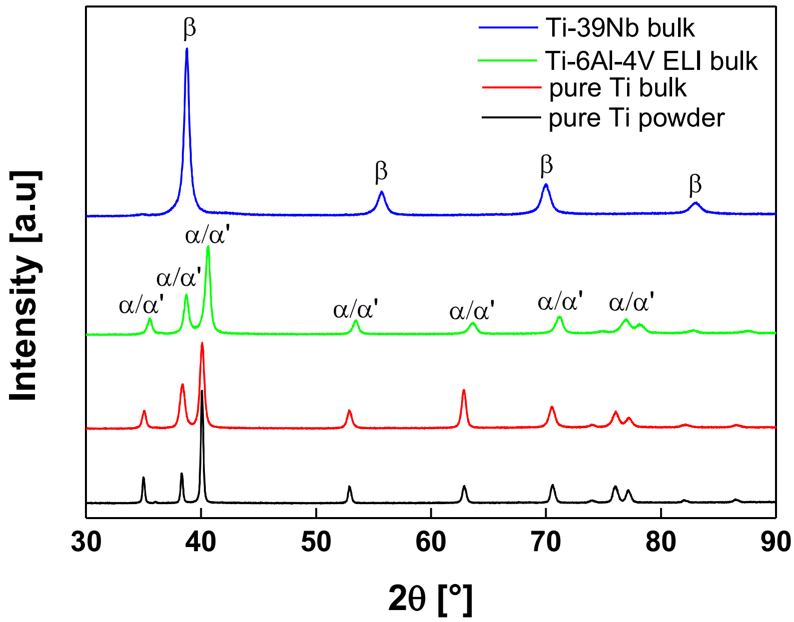

Figure 4.5 - XRD patterns of the Ti-based materials.

Optical micrographs analysis of the Ti alloys (Figure 4.6) obtained without contrast (part A, B and C), led to the conclusion that manufacturing defects were practically non-existent. In the bulk Ti alloys manufactured in the scanning direction (SD) and building direction (BD), only a few small gas pores were observed, structural integrity is negligible in Figure 4.7. In the porous Ti alloys, in addition to the occasional presence of gas pores, keyhole was identified, as show the Figure 4.4 (Arputharaj et al., 2025; Cao et al., 2021; Gökçe et al., 2025; Johannsen et al., 2023; H. Y. Ma et al., 2024; Ni et al., 2025; Soltani-Tehrani et al., 2023; K. Zhang et al., 2024; Zhuo et al., 2025).

After chemical etching with Kroll solution, it was possible to observe the different microstructures characteristic of each material in each direction SD and BD, as show the Figure 4.7. Pure Ti (Figure 4.7 (A) and (D)) has an essentially equiaxial microstructure, composed of small grains with well-defined contours (radius ranging from 1.1 to 9.3 μm). The predominant phase is α-Ti.

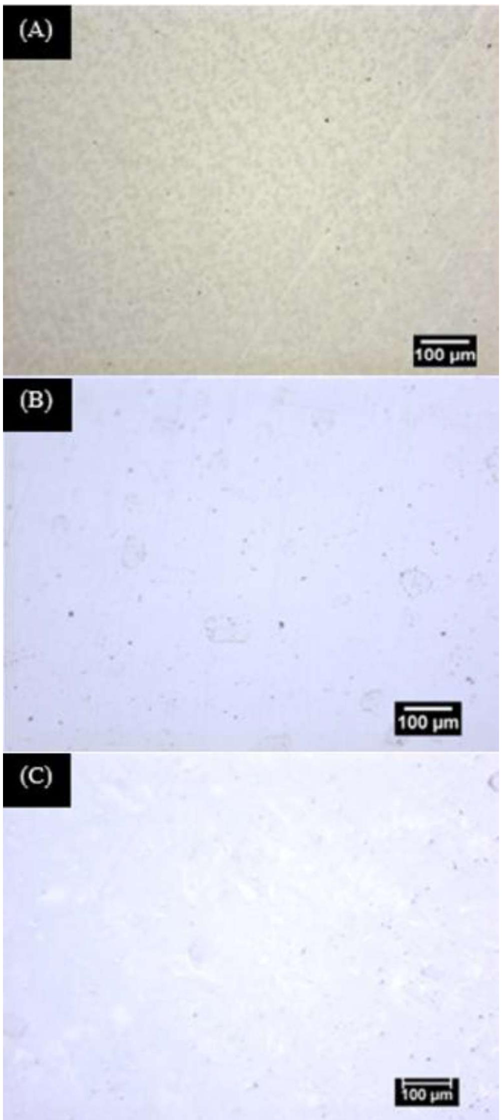

Figure 4.6 - Optical micrographs of the Ti alloys. Polished surface of (A) pure Ti, (B) Ti-6Al-4V, and (C) Ti-39Nb

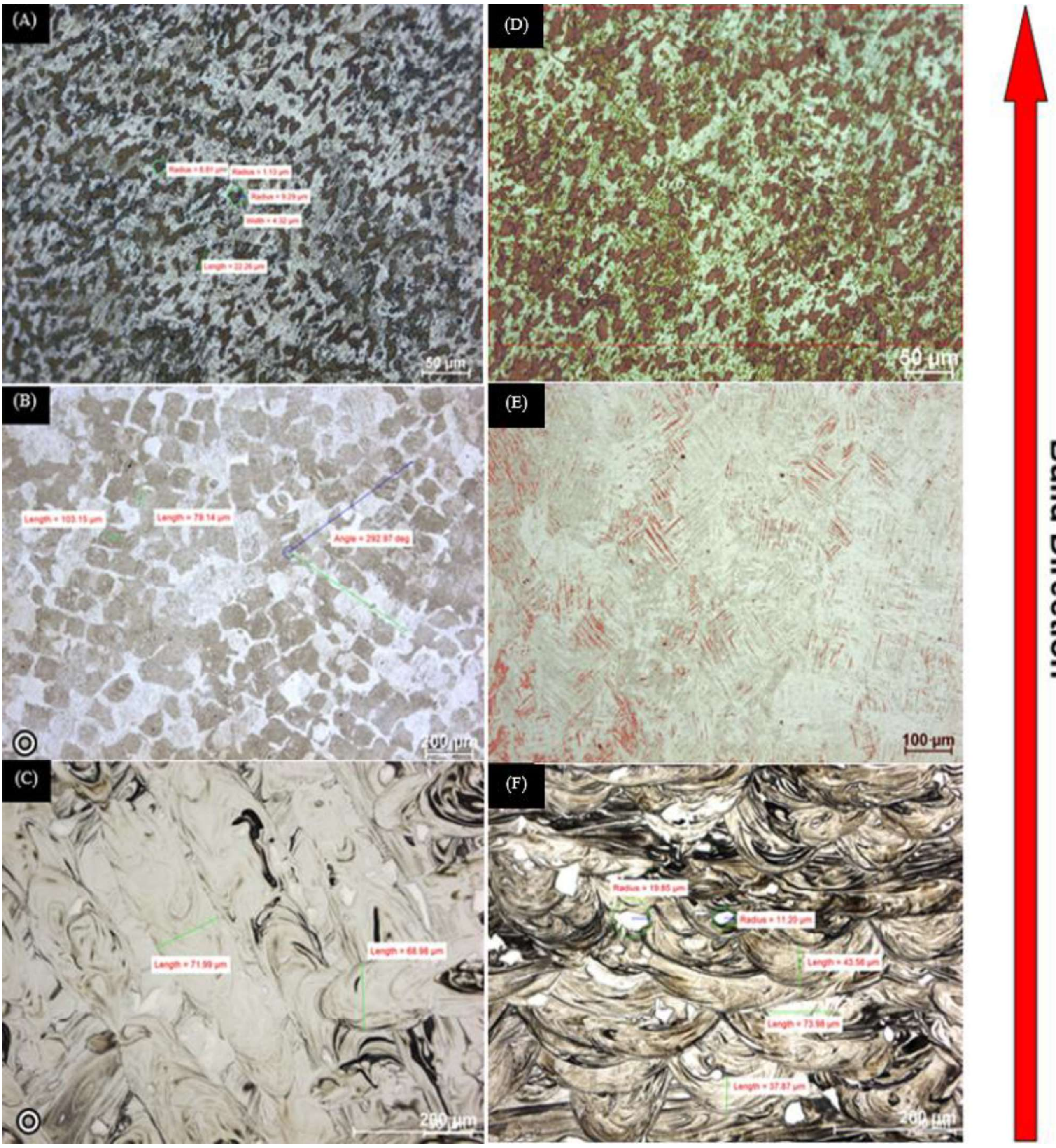

Figure 4.7 - Optical micrographs of the Ti alloys. Etched metallographic bulk materials in the scanning direction of (A) pure Ti, (B) Ti-6Al-4V, and (C) Ti-39Nb. Optical micrographs of the Ti alloys. Etched metallographic bulk materials in the building direction of (D) pure Ti, (E) Ti-6Al-4V and (F) Ti-39Nb.

The micrographs of the Ti-6Al-4V alloy are shown in Figure 4.7 (B) and (E). It may be the presence acicular α’ (as shown by DRX's analysis) in the microstructure of the alloy after L-PBF, although α-Ti and retained β-Ti have also been reported, the former visible as lighter regions and the latter as darker regions (Marin & Lanzutti, 2024). Inside the prior β phase grains, lamellar substructures are observed, compatible with the formation of martensitic α'. The size of the prior β grains is variable. This microstructure suggests an advantageous combination of mechanical strength (provided by the α' phase) and toughness (associated with the retained β phase).

The microstructure of the beta Ti-39Nb produced by L-PBF is presented in Figure 4.7 (C) and (F). The semi-circular melt pools (length of 69 to 72 μm) are clearly seen because of chemical micro segregation at the melt pool boundaries. It is also seen Nb particles (white regions) are not fully dissolved in the Ti-Nb matrix, which is related particle size of the pure Nb used to prepare the Ti-39Nb powder mixture, associated with the high melting temperature of pure Nb. The solidification substructure is not seen at this scale and was characterized by scanning electron microscopy (Figure 4.7). The high concentration of Nb (39 wt.%) gives the alloy significant β phase stabilization, resulting in a metastable β-Ti microstructure, which is associated with a reduced modulus of elasticity, a property that is particularly relevant for biomedical applications (Rodolfo Lisboa Batalha et al., 2020; Tang et al., 2024).

The analysis in BD corroborated previous observations and added complementary information about microstructural evolution. In the pure Ti bulk material (Figure 4.7 (A), the grain structure is predominantly equiaxial with the absence of extensive columns, which indicates a isotropic microstructure and a more homogeneous mechanical behavior across different directions. In the Ti-6Al-4V bulk material (Figure 4.7 (B), it was possible to identify the presence of banding and elongated prior β grains with length of approximately 137 μm, showing oriented structures with a Widmanstädter-type pattern (Singla et al., 2021). This preferred orientation induced by the solidification process promotes microstructural anisotropy, which tends to give the material a distinct mechanical property along the building and scanning directions. In the Ti-39Nb bulk material (Figure 4.7 (C), it was possible to clearly identify the orientation of the melt pools, with average dimensions of approximately 74 μm in length and 40 μm in width, directly reflecting the path followed by the laser beam during the manufacturing process. In addition, incompletely melted Nb particles were observed, whose irregular or polygonal morphology is indicative of local limitations in melting. The presence of these particles can influence both the microstructural homogeneity and the overall mechanical behavior of the alloy (David Deus Vilhena, 2021.; Singla et al., 2021).

The microstructure of the Ti alloys produced by L-PBF was further investigated by SEM (Figure 4.8). The pure Ti (SD – A and BD – B) presents a microstructure with grains of the stable α-Ti phase and plates of α'. This indicates that the rapid solidification conditions characteristic of the additive manufacturing process resulted in a microstructure with two phases as α' martensite is also formed.

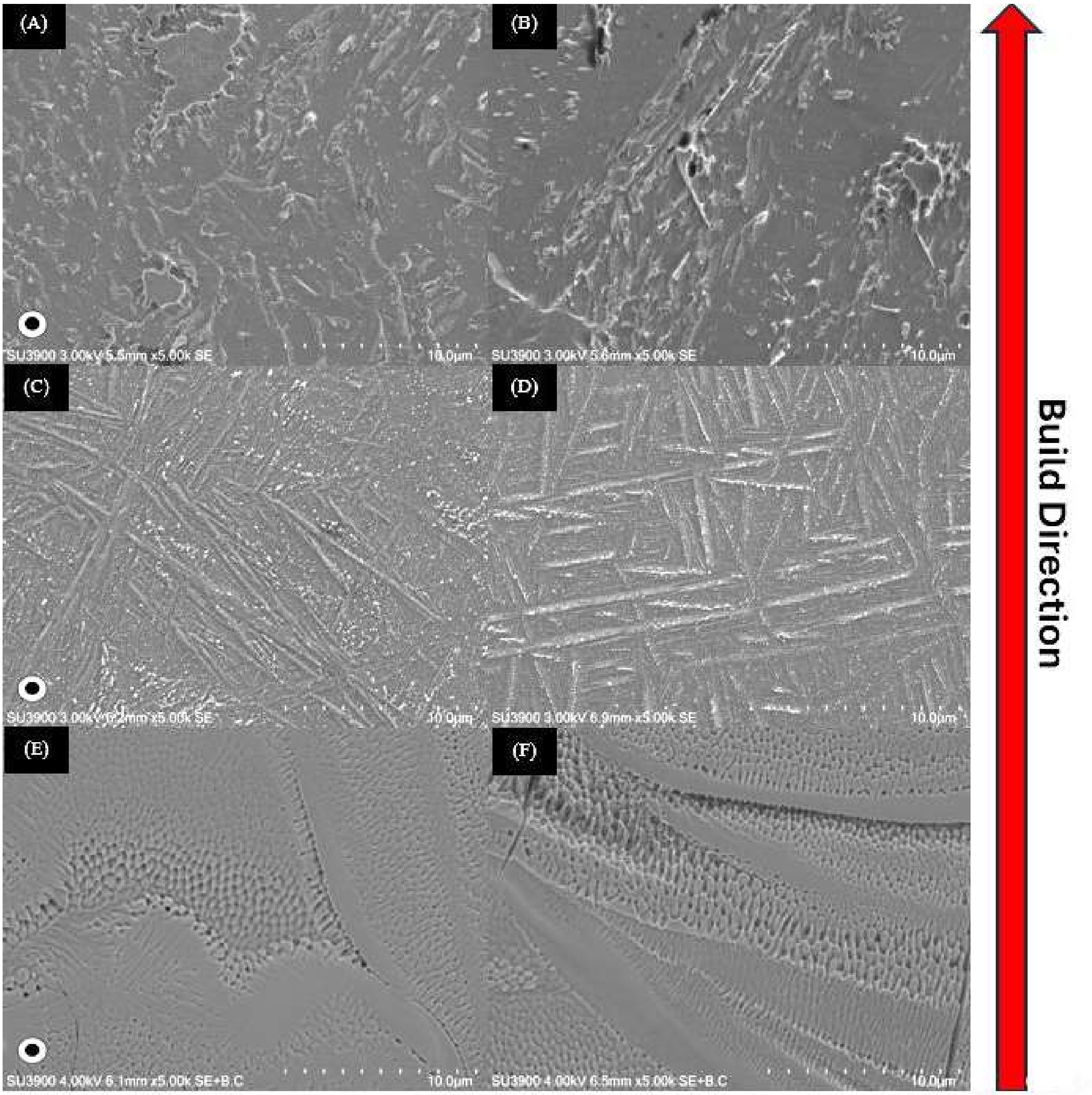

Figure 4.8 – SEM micrographs obtained in SD and BD, (A) pure Ti SD, (B) pure Ti BD, (C) Ti-6Al-4V SD, (D) Ti-6Al-4V BD, (E) Ti-39Nb SD, (F) Ti-39Nb BD.

The microstructure of the Ti-6Al-4V alloy (SD – (C) and BD – (D) present a predominantly acicular α' martensitic structure. The presence of the α´ phase, typical of rapid cooling processes in Ti alloys, is clearly observed, which confers greater mechanical strength but can also reduce ductility. This structural difference between pure Ti and Ti-6Al-4V demonstrates the versatility of Ti alloys in terms of controlling the relationship between process-microstructure-properties that is more suitable for biomedical applications, where a balance between strength, ductility and mechanical compatibility with bone is required (Bartolomeu et al., 2022; Noronha et al., 2023).

The Ti-39Nb alloy produced by L-PBF (SD – (E) and BD – (F) differ from the previous ones as a very fine cellular solidification structure is observed of a single beta phase microstructure. This single phase is more suitable for orthopedic applications since it results in a significantly lower elastic modulus and, therefore, greater biomechanical compatibility, as reported in the literature (Colombo-Pulgarín et al., 2021; Yue Li et al., 2026; Lisboa Batalha, 2019)

Figures 4.9, 4.10 and 4.11 present a surface analysis of the porous structures. In all the alloys – pure Ti, Ti-6Al-4V and Ti-39Nb, the manufacturing quality was considered acceptable since no significant defects are detected. Nonetheless, it was noticed powder particles sintered to the surface of the porous geometries, which is inherent to the powder-based nature of the L-PBF process (Bordbar-Khiabani & Gasik, 2023; Delpazir et al., 2023; Derimow et al., 2025; Fan et al., 2023; Memu et al., 2025; Senftleben et al., 2025; Sheremetyev et al., 2024; Shuvho et al., 2025; SITI NUR HAZWANI et al., 2022; B. Zhang et al., 2025; Zhao et al., 2021).

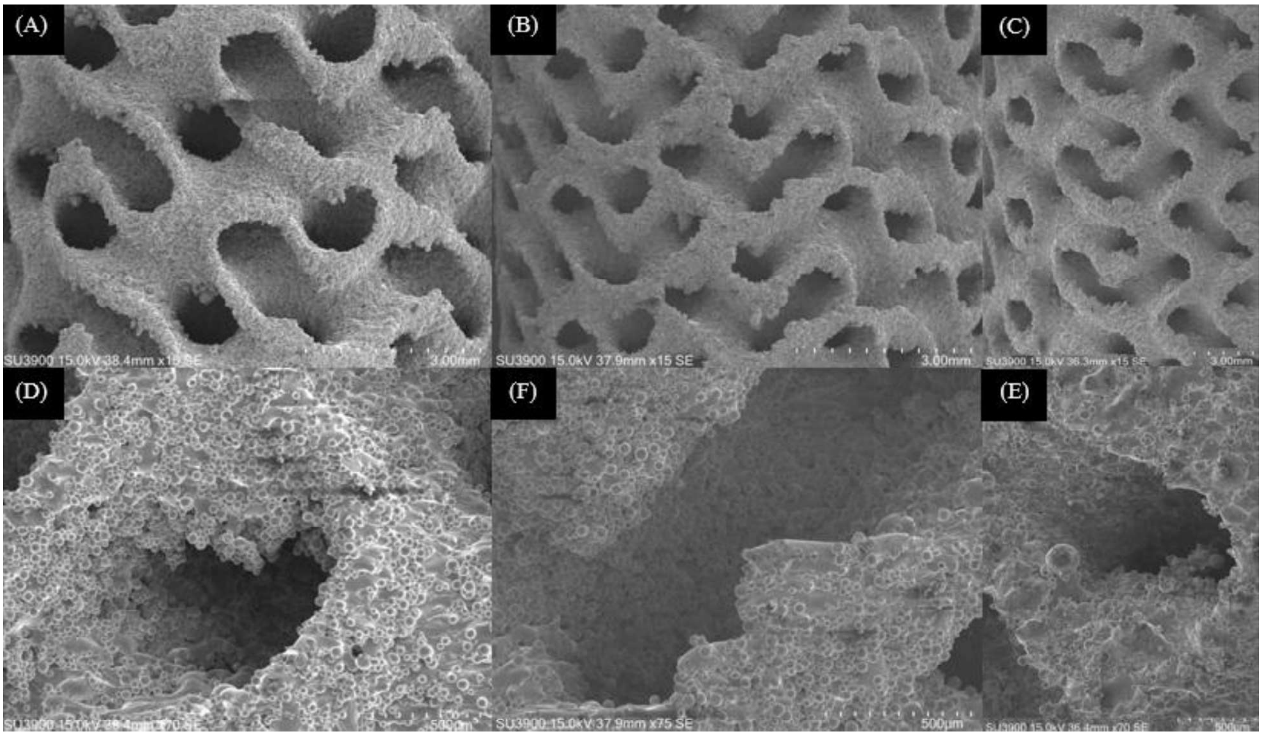

Figure 4.9 – Side analysis of gyroid geometry (65%) by SEM, (A) Pure Ti gyroid 65% side view, (B) Ti-6Al- 4V gyroid 65% side view, (C) Ti-39Nb gyroid 65% side view, (D) Pure Ti gyroid 65% pore side view, (E) Ti-6Al-4V gyroid 65% pore side view and (F) Ti-39Nb gyroid 65% pore side view.

The analysis of the structures revealed that the average pore size was approximately 500 μm in the Gyroid structures and equal to or smaller than 500 μm in the Voronoi structures, as illustrated in Figures 4.9, 4.10, and 4.11 parts (D), (F) and (E). These values fall within the dimensional range considered optimal for cell adhesion and proliferation (200–800 μm), highlighting the potential of these structures for applications in bone tissue engineering (Z. Chen et al., 2020; Dabaja et al., 2025; McGregor et al., 2021; Seehanam et al., 2024).

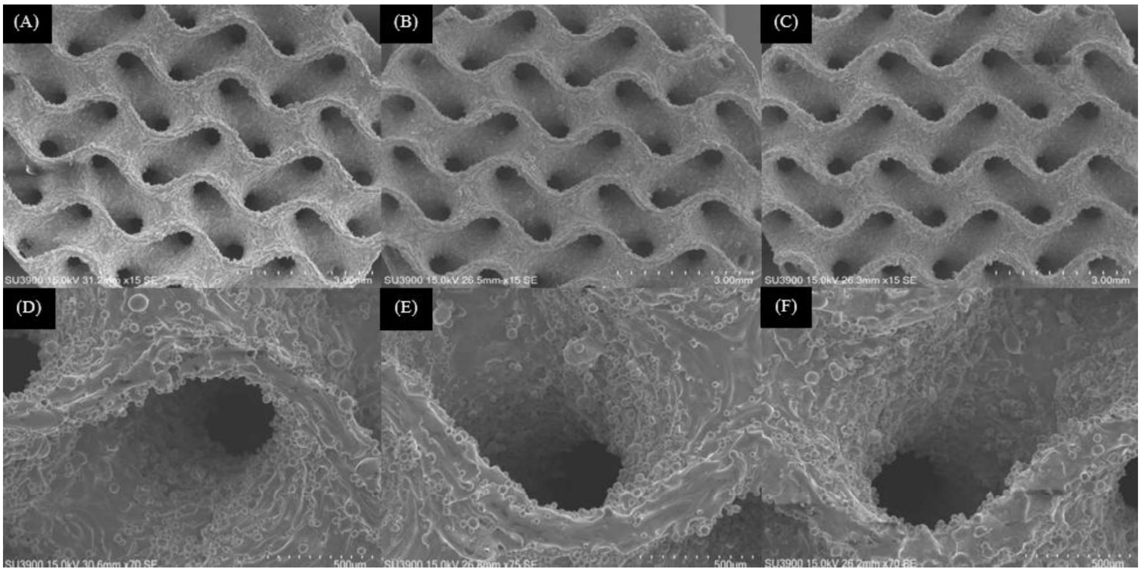

Figure 4.10 – Surface of gyroid geometry (65%) analysis by SEM: (A) pure Ti, (B) Ti-6Al-4V, (C) Ti-39Nb, (D) pure Ti pore surface, (E) Ti-6Al-4V pore surface and (F) Ti-39Nb pore surface.

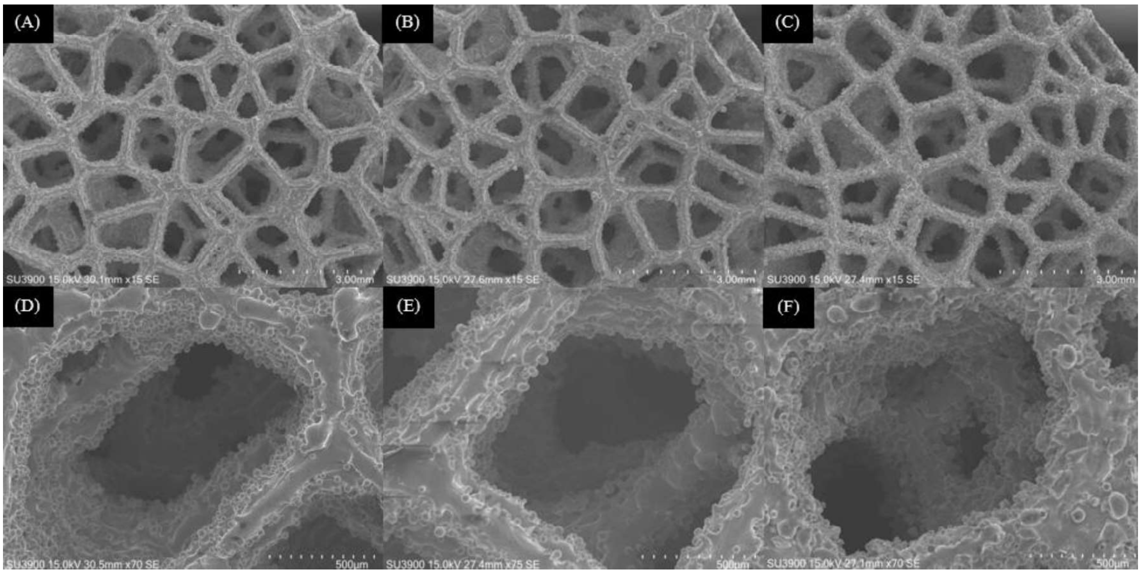

Figure 4.11 - Surface of Voronoi geometry (65%) analysis by SEM: (A) Pure Ti, (B) Ti-6Al-4V(C) Ti-39Nb, (D) pure Ti pore surface, (E) Ti-6Al-4V pore surface and (F) Ti-39Nb pore surface

4.5. Tensile properties

The comparative analysis of the tensile properties performed on horizontal (Figure 4.12 (A) and vertical (Figure 4.12 (B) build specimens of the Ti-based materials used (pure Ti, Ti-6Al-4V and Ti-Nb) shows marked differences in their mechanical behavior, which can be directly related to microstructure resulting from the L-PBF processing, according to the literature (Abd-Elaziem et al., 2024; Squillaci et al., 2025; C. Zhou et al., 2025).

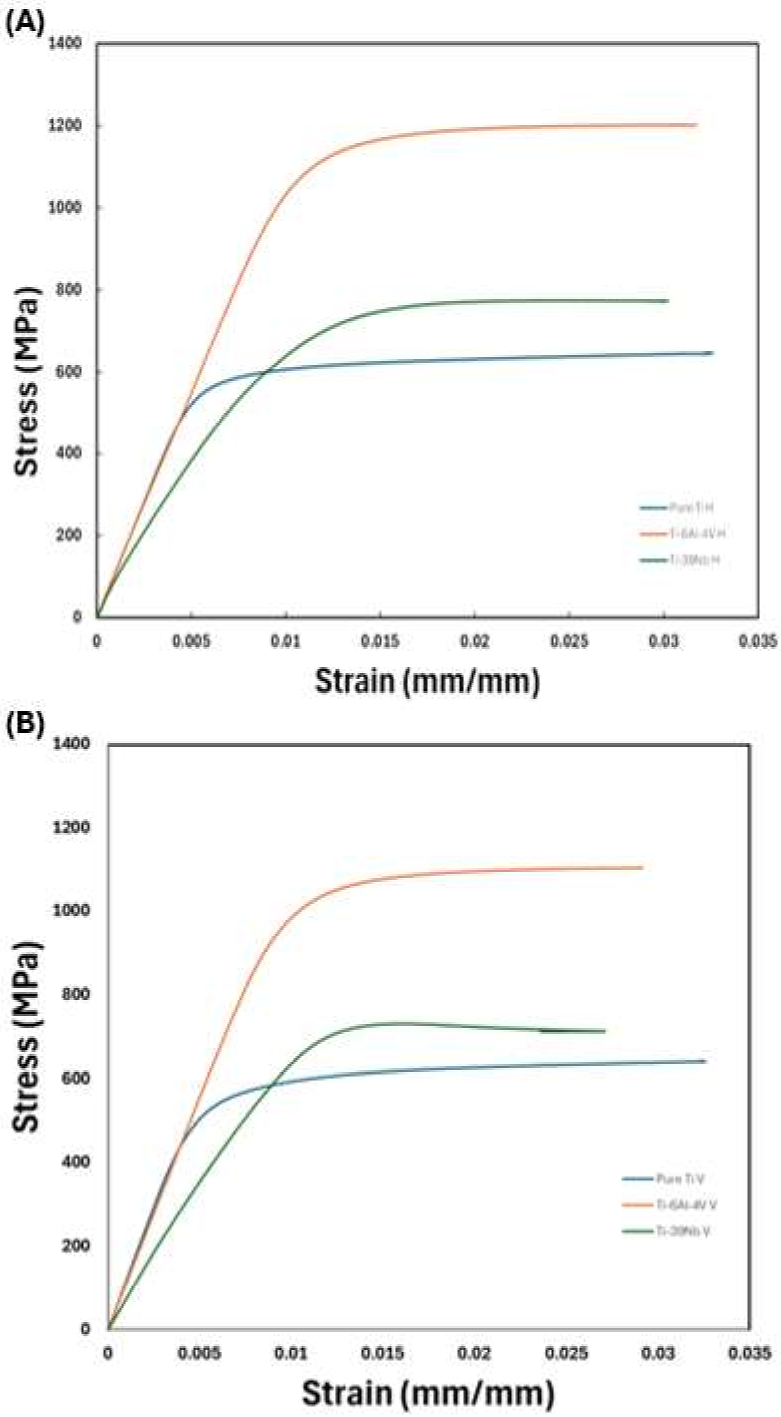

Figure 4.12 – Tensile stress – strain curves of representative specimens of the Ti alloys produced by L-PBF in the (A) horizontal and (B) vertical directions.

The stress-strain curves reveal clear differences in the initial slope (associated with the elastic behavior) and in the magnitude of the maximum stress reached. The Ti-39Nb specimens showed the lowest initial slope, confirming the reduced elastic modulus and anelastic behavior, while Ti-6Al-4V reached significantly higher stress levels, albeit with limited plastic deformation. Pure Ti showed higher plastic regimes, reflecting the greater ductility of the material. Comparison between orientations reveals that, although the differences between horizontal and vertical specimens are generally moderate, they are not negligible. In pure Ti and Ti-6Al-4V, the vertical orientation showed a slight increase in elongation, while in Ti-39Nb there was an increase in yield stress, accompanied by a reduction in elongation. These results suggest a contribution from microstructural anisotropy, possibly associated with the preferred grain direction or the morphology of the α and β phases (R L Batalha et al., 2022).

The tensile properties are summarized in Table 4.3. Regarding Young's modulus, it was observed that pure Ti and Ti-6Al-4V alloys presented values of 109 ± 1 GPa in horizontal direction (h) and 106 ± 3GPa in vertical direction (v), which are relatively close to the values reported in the literature for α and α+β alloys (106-110 GPa). The Ti-39Nb specimens, on the other hand, showed a significant smaller elastic modulus of 77 ± 2 GPa in the horizontal direction and 73 ± 4 GPa in the vertical direction, which represents a decrease of approximately 30% compared to the pure Ti and more conventional Ti-6Al-4V ELI alloy. This difference is particularly relevant in biomedical applications, since the lower modulus brings the material closer to human bone tissue (10–30 GPa), reducing the *stress shielding* effect and favoring load transfer for bone regrowth (Chmielewska & Dean, 2024).

Table 4.3 - Tensile properties values of pure Ti, Ti-6Al-4V ELI and Ti-39Nb alloys. H and V are the horizontal and vertical directions, respectively.

Specimen	Young`s modulus (GPa)	Tensile Strength (MPa)	Yield Strength (MPa)	Total Elongation (%)
Pure Ti (H)	109 ± 1	663 ± 33	553 ± 31	22 ± 1
Pure Ti (V)	106 ± 3	666 ± 21	553 ± 21	23 ± 2
Ti-6Al-4V ELI (H)	109 ± 1	1165 ± 53	1085 ± 48	10 ± 1
Ti-6Al-4V ELI (V)	106 ± 3	1117 ± 21	1041 ± 17	14 ± 1
Ti-39Nb (H)	77 ± 2	754 ± 18	619 ± 48	19 ± 3
Ti-39Nb (V)	73 ± 4	742 ± 11	703 ± 26	16 ± 1

In terms of tensile strength, the Ti-6Al-4V alloy showed highest ultimate tensile stress (UTS) of 1165 ± 53 MPa in the horizontal orientation (H) and 1117 ± 21 MPa in the vertical orientation (V). This behavior is accompanied by equally high yield stresses (approximately 1085 ± 48 MPa (H) and approximately 1041 ± 17 MPa (V)), reflecting the strengthening effect of the α' martensitic microstructure. Pure Ti presented the lowest tensile strength with a UTS of 663 ± 33 MPa (H) and 666 ± 21 MPa (V), and a yield strength of 553 ± 31 MPa (H) and 553 ± 21 MPa (V). The Ti-39Nb specimens exhibited intermediate strength, with average UTS of 754 ± 18 MPa (H) and 742 ± 11 MPa (V) and yield strengths between 619 ± 48 MPa (H) and 703 ± 26 MPa (V), similarly to previously reported in the literature (Jamshidi et al., 2020). The Ti-39Nb result is particularly interesting, since it is also accompanied by an intermediate ductility compared to the conventional Ti-6Al-4V ELI and pure Ti. Moreover, it is noted in the vertical orientation an increase in the yield strength compared to the horizontal specimens, suggesting anisotropy because of the L-PBF manufacturing process (Subramanian et al., 2025).

Regarding ductility as assessed by total elongation, the results show opposite trends between the materials. Pure Ti showed high of 22 ± 1 % (H) and 23 ± 2%(V), confirming its ductile behavior and with high deformation capacity before fracture. The Ti-6Al-4V ELI alloy, on the other hand, showed significantly lower ductility, with total elongation of 10 ± 1% (H) and 14 ± 1% (V), which is consistent with its high strength. The Ti-39Nb alloy showed again intermediate behavior, with total elongation of 19 ± 3% (H) and 16 ± 1% (V), reflecting a balanced combination of mechanical strength and ductility. It should be noted that, in all cases, the calculated standard deviations were relatively low, indicating good reproducibility of the tests and consistency of the results (Umbelino dos Santos et al., 2021).

The Ti-6Al-4V ELI alloy remains the most suitable for applications requiring high mechanical strength, albeit at the expense of reduced ductility. Pure Ti, on the other hand, is a more ductile material, albeit with lower strength, which can be advantageous in scenarios where deformability is critical. The Ti-39Nb alloy, on the other hand, is particularly promising for biomedical applications, combining intermediate mechanical strength, acceptable ductility and above all, a reduced Young's modulus that brings it closer to the mechanical properties of bone. The anisotropy identified between horizontal and vertical specimens reinforces the need for further studies to correlate microstructure with mechanical performance to optimize laser powder bed fusion processing conditions and ensure consistency in material properties regardless of part orientation.

4.5.1. Fractography analysis

Fractographic analysis was performed to understand the fracture mechanisms that occurred in the pure Ti, Ti-6Al-4V ELI, and Ti-39Nb tensile specimens and correlate with their microstructure and mechanical behavior. The evaluation was performed by scanning electron microscopy (SEM), with representative tensile specimens selected from each material and both horizontal and vertical orientations. The images obtained are presented in Figure 4.13 (A-L) highlighting the fracture surface characteristics of each material.

In general, the Ti-based alloys exhibited a predominantly ductile fracture, evidenced by the presence of well-defined dimples (coalescence cavities) on the fracture surface. These cavities result from the growth and coalescence of micro voids, typical of metallic materials subjected to significant plastic deformation prior to fracture. In all cases, the classic “cup and cone” morphology was observed, characteristic of ductile fractures under tensile loading, with a central region of necking accompanied by inclined edges. However, the extent of plastic deformation varied considerably between materials, reflecting the microstructural and phase differences of each alloy.

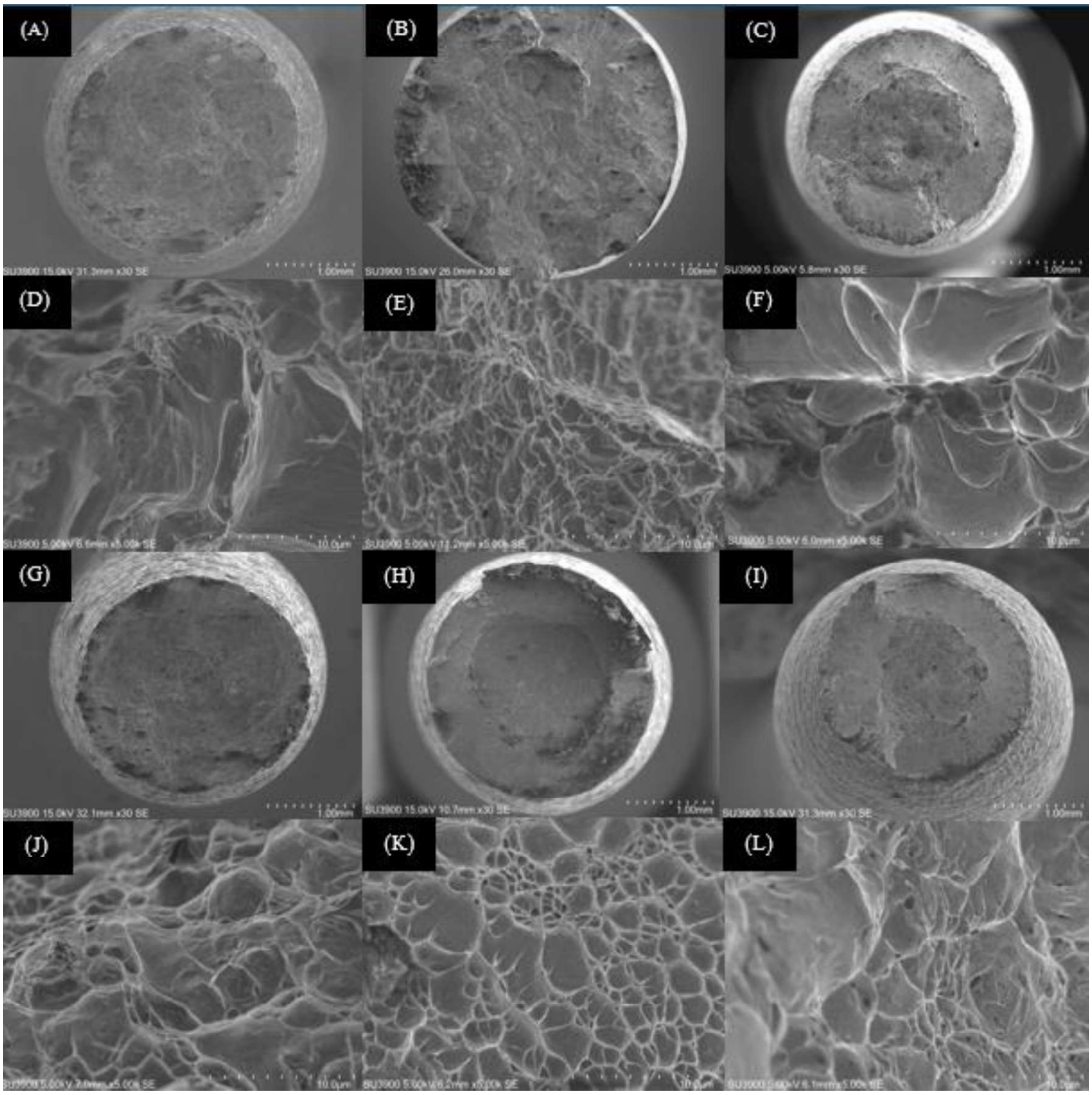

Figure 4.13 – Fracture surface of representative tensile specimens: (A), (D), (G) and (J) - Pure Ti; (B), (E), (H), (K) - Ti-6Al-4V; (C), (F), (I) and (L) - Ti-39Nb.

The pure Ti presented a fracture surface with large, uniformly distributed dimples, indicating high plasticity prior to fracture. The presence of pronounced necking in the gauge section confirmed this behavior. Comparative analysis between horizontal and vertical tensile specimens revealed marked similarities in fracture morphology, although vertical tensile specimens showed slightly greater elongation before fracture, possibly due to the more favorable orientation of the layers relative to the loading axis. In the case of pure Ti in the horizontal direction (Figure 4.13 (A) and (D), a fracture surface with larger cavities and preferential elongation of the dimples was observed, suggesting strong anisotropy and localized plastic deformation capacity. The presence of fibrous ligaments and lamellar zones indicates high overall ductility, consistent with the expected behavior of commercially pure Ti with a single-phase α-Ti structure. Pure Ti in the vertical direction (Figure 4.13 (G) and (J), showed a more homogeneous distribution of cavities, with more equiaxial and larger dimples compared to the horizontal direction, reflecting high ductility and confirming the influence of processing orientation on tensile behavior. Thus, for pure Ti, it is observed that both directions reveal ductile fracture, although the horizontal orientation favors the formation of elongated ligaments due to the crystallographic texture. The α-Ti microstructure typical of pure Ti, previously observed by optical microscopy and SEM, explains the high ductility (Xiao et al., 2023).

In the Ti-6Al-4V ELI alloy, fractography revealed mixed fracture characteristics, with predominantly ductile zones interspersed with localized areas of quasi-brittle fracture (Figure 4.13 (B) and (H)). The ductile regions had smaller and shallower dimples than those observed in pure Ti, while the brittle zones exhibited flat facets and evidence of localized cleavage, particularly in specimens manufactured in the vertical orientation (Figure 4.13 (B) and (H)). Analysis of Ti-6Al-4V in the horizontal direction (Figure 4.13 (B) and (E) revealed a high density of very fine, shallow dimples distributed uniformly. Although this morphology is typical of ductile fracture by coalescence of micro voids and the small size of the dimples indicates a lower capacity for local plastic deformation before fracture. The same behavior was observed in the vertical direction (Figure 4.13 (H) and (K), reinforcing the idea that the presence of the α' and residual α+β microstructure that resulted in a high strength also reduced ductility of the alloy. The overall result is a partially ductile and partially brittle fracture, with less necking and less total elongation compared to pure Ti and Ti-39Nb. In addition, specimens with horizontal orientation showed greater homogeneity on the fracture surface, suggesting better cohesion between layers and less influence from discontinuities generated during the L-PBF process (Xiao et al., 2023).

The Ti-39Nb alloy showed a clear ductile fracture, with a dense distribution of small and medium-sized dimples, randomly oriented and predominantly hemispherical in shape. This morphology indicates marked and progressive plastic deformation up to fracture, consistent with the high elongation measured in the tensile tests. The β single phase microstructure of the Ti-39Nb processed by L-PBF was responsible for this behavior. Additionally, no signs of intergranular fracture or cleavage regions were observed, confirming the high toughness of the alloy and its resistance to crack propagation. In terms of manufacturing orientation, the horizontal and vertical specimens presented similar morphologies, demonstrating that the more homogeneous and isotropic microstructure of Ti-39Nb minimizes the influence of orientation in the mechanical properties of the alloy. In the horizontal direction (Figure 4.13 (C) and (F), the fracture surface showed larger and deeper dimples, some in the shape of "petals" (Figure 4.13 (F), evidencing the growth and coalescence of micro voids more pronounced than in the Ti-6Al-4V ELI alloy. In the vertical direction (Figure 4.13 (I) and (L), larger and deeper cavities were also observed suggesting again a high capacity for plastic deformation before fracture. This behavior is consistent with the literature, which associates Nb-stabilized β Ti alloys with greater overall ductility that favors the mobility of dislocations and homogeneous plastic deformation before fracture (Brodie et al., 2020; McConnell et al., 2025; Ummethala et al., 2020).

In general, the comparison between the different materials produced by L-PBF with different orientations shows that the Ti-6Al-4V ELI alloy exhibited more consistent with its higher strength and lower ductility, whereas pure Ti revealed a largely ductile fracture, albeit with lower overall strength, while the Ti-39Nb combined superior ductility with homogeneous and progressive fracture, showing mechanical behavior closer to that of cortical bone. These results reinforce the suitability of Ti-39Nb alloy as a promising material for biomedical applications, particularly in orthopedic implants, where a ductile, stable and predictable fracture mechanism is desirable to minimize the risk of catastrophic failure.

4.6. Compressive properties

Compression tests were performed on bulk cylinders as well as cylinders with Voronoi and gyroid porous structures and three porosity levels (50%, 65% and 75%), as shown in Figures 4.14 and 4.15 and 4.16. The results are summarized in Table 4.4. Similarly to the tensile tests, analysis of the curves corresponding to the bulk materials shows that Ti-6Al-4V exhibits highest compressive strength, withstanding a maximum load of approximately 95 kN. Commercially pure Ti showed the lowest compressive strength, with a maximum load of approximately 54 kN, while the Ti-39Nb alloy showed intermediate behavior, with a maximum compressive load up to 61 kN (Figure 4.14).

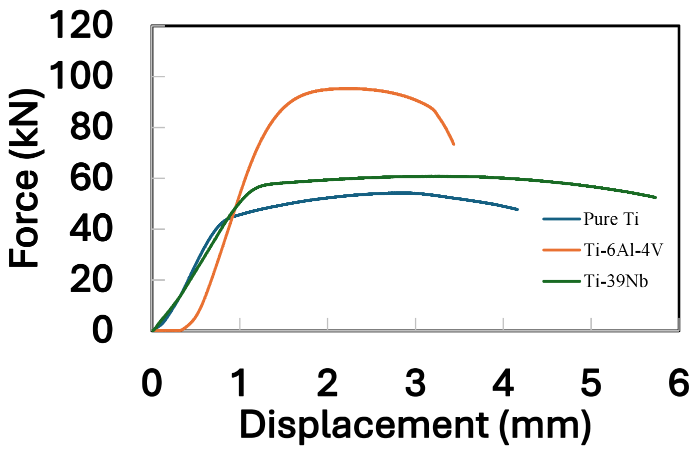

Figure 4.14 - Compression curves of bulk materials

When the porous geometries were tested, a significant reduction in overall stiffness and an increase in apparent ductility are observed. In the gyroid geometry with 50% porosity of pure Ti and Ti-39Nb, maximum compressive loads of approximately 28 kN and 24 kN, respectively, while Ti-6Al-4V reached about 49 kN but exhibited premature fracture (Figures 4.15 and 4.16 (A)). This behavior resulted in deformation limited to 6%, unlike the other bulk materials, which reached average values of 33%, thus demonstrating a generally more ductile behavior than the bulk materials. For the gyroid geometry with 65% porosity, there was a marked reduction in load capacity: Pure Ti withstood loads up to 8 kN, Ti-39Nb up to 12 kN and Ti-6Al-4V up to 14 kN. For gyroid 75% porosity, the maximum force values were around 3 kN (Pure Ti), 6 kN (Ti-39Nb) and 8 kN (Ti-6Al-4V). These results demonstrate that, although increased porosity leads to a marked reduction in stiffness and compressive strength, the deformability and homogeneous distribution of stresses (Figure 4.14, 4.15, 4.16 and table 4.4) in the gyroid geometry promote a more stable response to loading, reflecting highly ductile behavior (Figure 4.15). However, such high levels of porosity make these structures unsuitable for significant load-bearing applications, such as structural implants, despite the benefits in terms of lightness and permeability.

Table 4.4 – Compression load and displacement of cylinders of pure Ti, Ti-6Al-4V ELI and Ti-39Nb produced by laser powder bed fusion.

Material	Structure	Maximum compression load (kN)	Maximum displacement (mm)
Pure Ti	Bulk	54 ± 1	4±0
	Gyroid 50%	28 ±2	10±0
	Gyroid 65%	8 ±1	10±0
	Gyroid 75%	3 ±1	10±0
	Voronoi 50%	12 ±1	10±0
	Voronoi 65%	6 ±1	10±0
	Voronoi 75%	2 ±1	10±0
Ti-6Al-4V ELI	Bulk	95 ±2	2±1
	Gyroid 50%	49 ±2	2±0
	Gyroid 65%	14 ±1	10±0
	Gyroid 75%	8 ±2	10±0
	Voronoi 50%	25 ±2	10±0
	Voronoi 65%	14 ±1	10±0
	Voronoi 75%	6 ±1	10±0
Ti-39Nb	Bulk	61 ±4	6±1
	Gyroid 50%	24 ±3	10±0
	Gyroid 65%	12 ±2	10±0
	Gyroid 75%	6 ±1	10±0
	Voronoi 50%	20 ±2	10±0
	Voronoi 65%	8 ±1	10±0
	Voronoi 75%	1 ±0	10±0

Regarding the Voronoi structures, their overall mechanical behavior is less rigid than that of gyroid, although the scaffolds have similar ductility. Voronoi Structure has shown a disadvantage from a structural point of view. For Voronoi with 50% porosity, pure Ti withstood approximately 12 kN, while Ti-39Nb showed a maximum compression load of 20 kN, and Ti-6Al-4V approximately 25 kN of maximum load, showing a substantial decrease compared to gyroid with the same porosity fraction. In Voronoi with 65% porosity, the maximum compression loads were 6 kN for pure Ti, 8 kN for Ti-39Nb, and 14 kN for Ti-6Al-4V. Finally, for porosity of 75%, even lower values were recorded: approximately 2 kN (Pure Ti), 1 kN (Ti-39Nb) and 6 kN (Ti-6Al-4V).

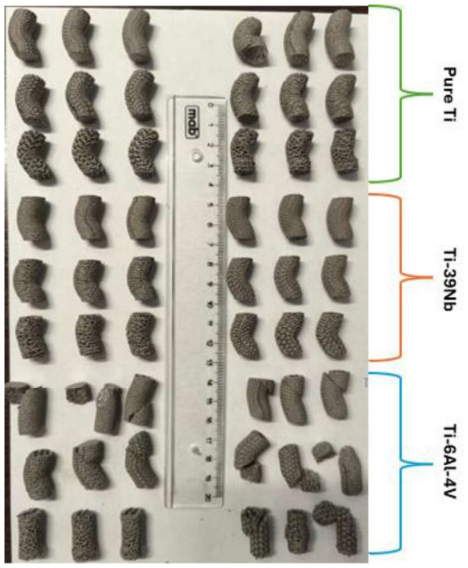

Figure 4.15 - Structures after compression tests organized by material (pure Ti, Ti-39Nb and Ti-6Al-4V ELI), with the porous geometries (gyroid and Voronoi) and porosity level (50%, 65% and 75%).

In most cylinders' porous structures, an initial peak load is observed, followed by a plateau region where the load stabilizes or decreases slowly as the structure progressively deforms. In other cases, especially in Voronoi and Ti-6Al-4V cylinders, abrupt drops in the compression load occur, indicating localized collapse or fracture of structural elements of the porous geometry. In general, increasing porosity reduces the peak load and energy absorbed until densification. The geometry of the porous structure also strongly influenced the response to compression, with gyroid structures tending to exhibit higher peaks and smoother plateaus (more homogeneous load distribution), while the cylinders with Voronoi structure showed more heterogeneous responses with localized collapses (Bora et al., 2023; Yongyue Li et al., 2024; Peng et al., 2024; Rehman et al., 2025).

Pure Ti and Ti-39Nb alloys generally showed a more ductile and stable behavior, without the marked presence of successive peaks and valleys. In contrast, the Ti-6Al-4V alloy exhibited marked and repeated oscillations in the load-displacement curve of the porous cylinders, characteristic of a progressive and discontinuous collapse of the structure. These oscillations (reflected by peaks and valleys) are related to a process of loss and regaining of load support throughout the compression test, suggesting that the Ti-6Al-4V suffered multiple localized failures and internal stress redistributions. This behavior is associated with the more brittle nature of the material, possibly due to the presence of the martensitic α′ (alpha line) phase, as observed in the Ti-6Al-4V without subsequent heat treatment. The formation of α′ Ti-based materials leads to higher mechanical strength, but also to reduced ductility, a factor that favors sudden fractures in regions of high stress concentration. This phenomenon explains the irregular pattern observed: as thinner structural elements are compressed, the curves show a peak; when connections within the structure fracture, there is an abrupt drop (valley), with the load being transferred to other regions of the structure that are still intact, giving rise to new peaks and valleys in sequence.

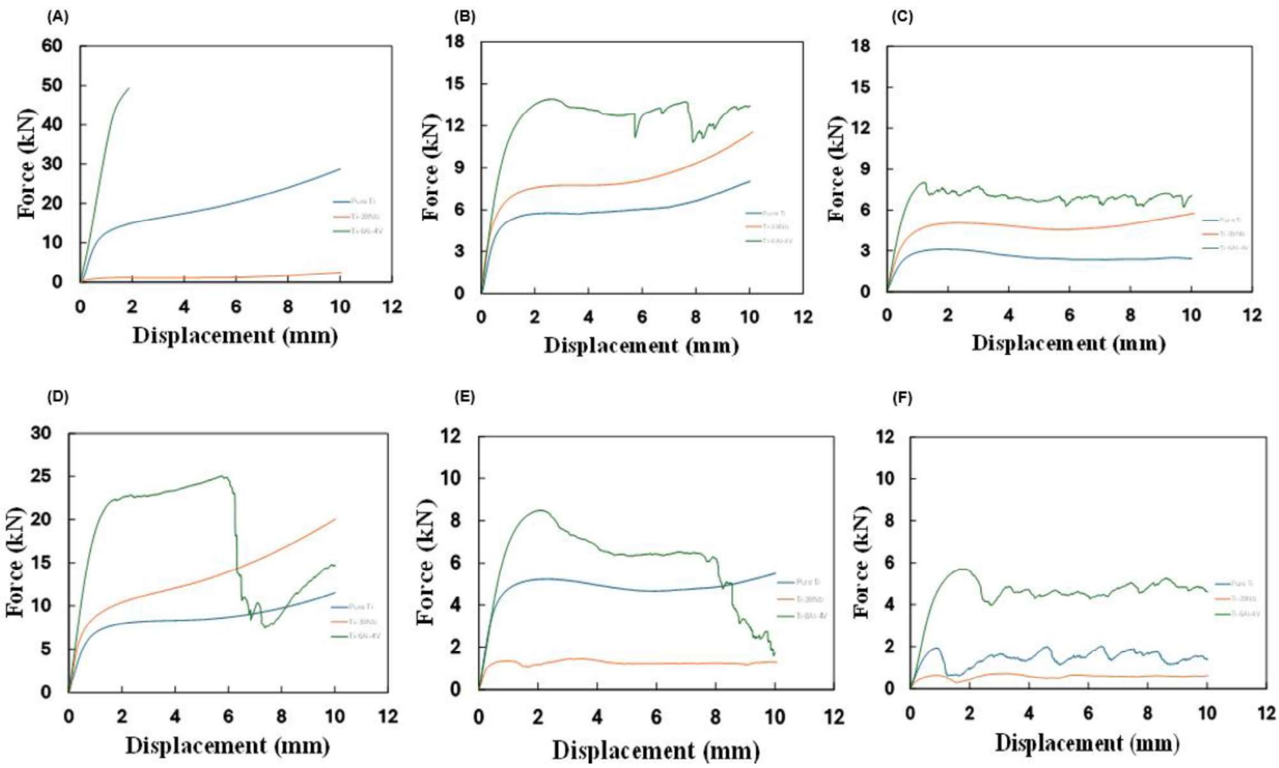

Figure 4.16 – Compression curves of (A) gyroid with 50% porosity (B) gyroid with 65% porosity (C) gyroid with 75% (D) Voronoi 50% porosity (E) Voronoi 65% porosity (F) Voronoi 75% porosity. Blue, green, and orange curves are pure Ti, Ti-6Al-4V ELI and Ti-39Nb alloys, respectively.

The SEM images of the cylinders with Voronoi and gyroid porous structured, organized by material, is shown in Figures 4.17 and 4.18, confirming the failure modes inferred from the curves.

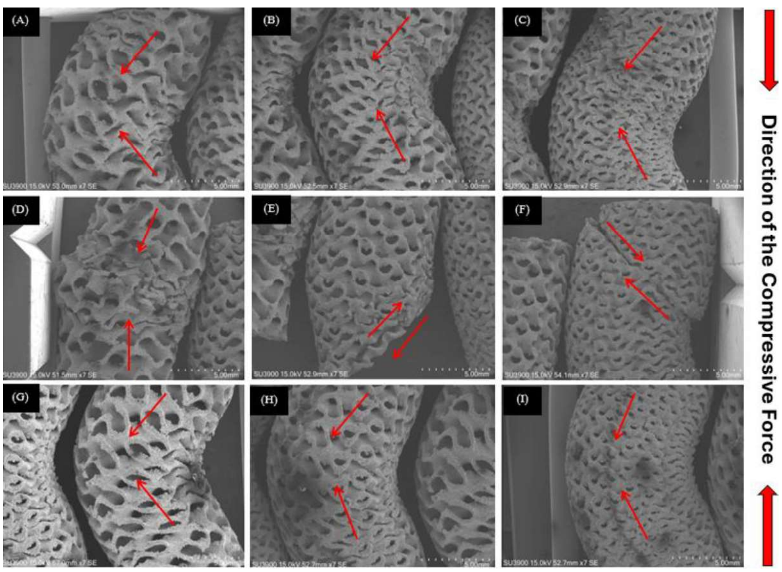

Figure 4.17 –The effects of the load exerted in the compression test on each gyroid structures: (A) pure Ti gyroid 75%, (B) pure Ti gyroid 65%, (C) pure Ti gyroid 50%, (D) Ti-6Al-4V gyroid 75%, (E) Ti-6Al-4V gyroid 65%, (F) Ti-6Al-4V gyroid 50%, (G) Ti-39Nb gyroid 75%, (H) Ti-39Nb gyroid 65%, (I) Ti-39Nb gyroid 50%.

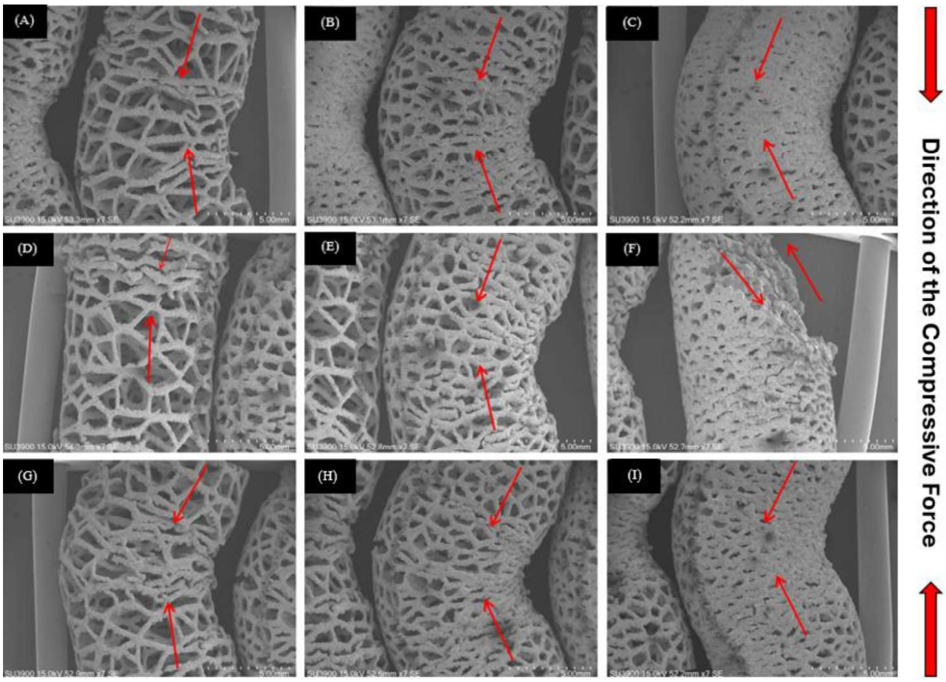

Figure 4.18 - The effects of the load exerted in the compression test on each Voronoi structures: (A) pure Ti Voronoi 75%, (B) pure Ti Voronoi 65%, (C) pure Ti Voronoi 50%, (D) Ti-6Al-4V Voronoi 75%, (E) Ti-6Al-4V Voronoi 65%, (F) Ti-6Al-4V Voronoi 50%, (G) Ti-39Nb Voronoi 75%, (H) Ti-39Nb Voronoi 65%, (I) Ti-39Nb Voronoi 50%.

In the pure Ti geometries (Figure 4.17 (A), (B) and (C) and Figure 4.18 (A), (B) and (C), the images show structures with surface roughness, but without massive fracture. The faces remain parallel to each other, and on one side of the structure, the pores were compressed-closed, while on the other side, they were open, causing some to fracture. This is consistent with deformation due to curvature of the structures and intermediate behavior in the curves (moderate peaks and plateaus without catastrophic drops). On the other hand, for Ti-6Al-4V (Figure 4.17 (D), (E) and (F) and Figure 4.18 (D), (E) and (F), the images show areas with fragmentation and debris at the interface between pores, and the junction surfaces appear with fractured areas. These characteristics explain the sudden drops in force observed in several curves (collapse due to fracture). The microstructure resulting from L-PBF and the possible increase in local fragility favor fracture rather than deformation. Finally, the Ti-39Nb structures (Figure 4.17 (G), (H) and (I) and Figure 4.18 (G), (H) and (I), through SEM image analysis, compressed and bent structures are observed without abrupt fractures. The surface appears less fragmented, which explains the smoother compression load-displacement curves and indicates good energy dissipation, having a more progressive and ductile behavior (Lisboa Batalha, 2019).

Each combination of material-geometry-porosity has clinical advantages and disadvantages. The Ti-6Al-4V ELI alloy demonstrated high compressive strength and potential for use in locations and applications subject to high loads, however, the risk of localized failure and stress shielding due to its high modulus is notable. Pure Ti exhibits worst behavior of these three materials, but it is an excellent choice for implants, so much so that there are implants already manufactured with pure titanium, such as hip implants and heart valves. Finally, the beta Ti-39Nb alloy has the most ductile behavior with the lowest Young's modulus of the investigated materials, indicating a reduced risk of *stress-shielding* and offering good energy absorption, which are desirable characteristics for implants aimed at bone integration. However, attention must be paid to the load applied (D. Chen et al., 2022; H. H. Cheng et al., 2024; González-Guillén et al., 2024; Rehman et al., 2024). Regarding the porous structure, gyroid geometry, because it distributes stress evenly, is preferable for implants that require structural safety, unlike Voronoi geometry, which can be used where controlled collapse or greater permeability is desired, but requires reinforcement in critical regions (Issariyapat et al., 2023). Finally, the internal and surface quality of the porous structures should be taken into account, together with the process-microstructure-property relationship obtained when such geometries of biocompatible Ti-based alloys are produced using laser powder bed fusion (Araya et al., 2024; B. Deng et al., 2025; Gandhi et al., 2025; Herath et al., 2021; J. Li et al., 2024; Papazoglou et al., 2024; Zluhan et al., 2025)

Chapter 5
Conclusions

This chapter presents the final conclusions obtained from the comparative study carried out with three biocompatible materials (pure Ti, Ti-6Al-4V and Ti-39Nb), in combination with two different geometries (Voronoi and Gyroid) and different levels of porosity (50%, 65% and 75%) and produced by laser powder bed fusion (L-PBF). The integrated analysis of these factors demonstrated their impact on mechanical, microstructural and functional properties, with a special focus on their suitability for application in orthopedic implants. Based on the results obtained by microstructural analyses (OM and SEM-EDS), mechanical tests (tensile and compression) and fractography analyses (SEM), it was possible to identify the advantages and limitations of each material and geometric configuration, providing a critical and informed view of their potential in the biomedical context.

From the microstructural analysis, it was concluded that pure titanium exhibited a predominant α phase, Ti-6Al-4V presented a dual α+β microstructure, and Ti-39Nb showed a single β phase. The presence of the β phase in Ti-39Nb resulted in enhanced ductility, highlighting its potential suitability for biomedical implant applications.

The results of the tensile tests showed significant differences between the three alloys studied, reflecting the impact of microstructure and chemical composition on mechanical properties. The Ti-6Al-4V ELI (Gr23) alloy had the highest mechanical strength values, with UTS = 1165 ± 53 MPa (H) and 1117 ± 21 MPa (V), and YS = 1085 ± 48 MPa (H) and 1041 ± 17 MPa (V), besides the highest stiffness with Young's modulus of 109 ± 1 GPa (H) and 106 ± 3 GPa (V), confirming its more rigid and resistant nature, although accompanied by lower ductility (10 ± 1% (H) and 14 ± 1% (V)). Pure Ti (Gr2) presented similar Young's modulus (109 ± 1 GPa (H) and 106 ± 3 GPa (V)), but with lower tensile strength (UTS = 663 ± 33 MPa (H) and 666 ± 21 MPa (V); YS = 553 ± 31 MPa (H) and 553 ± 21 MPa (V)). On the other hand, it stood out for its high ductility, with elongations of 22 ± 1% (H) and 23 ± 2% (V). The Ti-39Nb alloy showed an optimal compromise between stiffness, strength and ductility. The Young's modulus was 77 ± 2 GPa (H) and 73 ± 4 GPa (V), which is significantly closer to that of cortical bone (~10 GPa).

In compression tests, the bulk Ti alloys showed greater strength and stiffness, with none reaching the imposed deformation limit (33%). The average yield stress values were 688 ± 6 MPa (pure Ti), 1237 ± 19 MPa (Ti-6Al-4V) and 748 ± 41 MPa (Ti-39Nb), confirming the greater strength of Ti-6Al-4V, the superior ductility of Ti-39Nb and the lower strength of pure Ti. With the introduction of porous structures, a marked reduction in stiffness and maximum supported compression load was observed, proportional to the level of porosity. In gyroid structures with 50% porosity, the maximum loads reached approximately 28 kN (pure Ti), 24 kN (Ti-39Nb), and 49 kN (Ti-6Al-4V). With 65% porosity, the values decreased to 8 kN (pure Ti), 12 kN (Ti-39Nb) and 14 kN (Ti-6Al-4V), while at 75% porosity they reached 3 kN (pure Ti), 6 kN (Ti-39Nb) and 8 kN (Ti-6Al-4V). Despite the decrease in the compression resistance with increasing porosity, the gyroid geometries exhibited more stable behavior, characterized by progressive collapse, homogeneous stress distribution and greater energy absorption capacity. On the other hand, Voronoi structures exhibited lower rigidity and localized collapses, a consequence of geometric irregularity and the concentration of stresses on the most fragile connections. At 50% porosity, the maximum loads were 12 kN (pure Ti), 20 kN (Ti-39Nb) and 25 kN (Ti-6Al-4V); at 65%, 6 kN (pure Ti), 8 kN (Ti-39Nb) and 14 kN (Ti-6Al-4V); and at 75%, 2 kN (pure Ti), 1 kN (Ti-39Nb) and 6 kN (Ti-6Al-4V).

Regarding the raw materials used in L-PBF processing, it was noticed that the pure Ti and Ti-6Al-4V powders had a predominantly spherical morphology, while the mixture for Ti-39Nb contained irregular Nb particles. However, the mechanical properties weren't affected.

In fractographic analysis, the Ti-39Nb alloy exhibited ductile fracture behavior, characterized by deep and extensive dimples, confirming its high plastic deformation capacity prior to rupture. Ti-6Al-4V, on the other hand, exhibited more brittle behavior, consistent with its α' microstructure. Thus, beta-Ti alloy such as Ti-39Nb is a promising candidate for load-bearing implants, reducing the risks of implant rejection and failure.

The Ti-39Nb offered superior mechanical performance under compressive stress, making it ideal for high-stress and load-bearing applications. Provided good mechanical strength and ductility but with a lower UTS, which may be advantageous for initial bone integration but needs careful management to avoid long-term mechanical implant performance. The Ti–6Al–4V alloy showed higher strength but lower ductility. Pure Ti presented the lowest strength and the highest ductility, indicating that its use as structural implant is strongly dependent on the loads involved.

Porous structures, especially the gyroid, showed significant potential in achieving elastic modulus even closer to cortical bone, while maintaining adequate mechanical strength. The geometric continuity of gyroid favors load transfer, thus representing a safety factor. On the other hand, Voronoi structures showed to have inferior mechanical properties to gyroids in all fields and are therefore not recommended for use in lifetime or long-life implants.

The L-PBF technology was proven to be an effective manufacturing route with great potential to produce geometrically complex parts of beta Ti alloys, allowing for porosity control and implant customization. Despite inherent challenges, such as residual stress and local heterogeneities, that technology has demonstrated feasibility for biomedical applications, mainly due to its high level of precision and freedom to produce customized geometries. New parameters must be continuously investigated to improve the mechanical behavior of these alloys.

In summary, it can be concluded that the Ti-39Nb alloy, manufactured by L-PBF combined with an engineered porosity with gyroid 65% architecture, is a technically promising solution for orthopedic implants, reducing the stress shielding effect without compromising mechanical integrity. The significant reduction in the modulus of elasticity (77 ± 2 GPa in the horizontal orientation and 73 ± 4 GPa in the vertical orientation) and the high ductility confirms that the Ti-39Nb alloy is a viable alternative to traditional Ti-6Al-4V, especially in contexts with intermediate loads that require biomechanical compatibility between the implant and the bone.

Finally, this study reinforces the importance of research into titanium β alloys and customized porous structures produced by additive manufacturing, paving the way for future work aimed at optimizing manufacturing parameters, *in vitro* and *in vivo* evaluation of biological response, and the development of implants with superior mechanical and clinical performance. Further research is recommended to explore advanced surface modification techniques, such as nano-structuring or coatings, to further enhance biocompatibility and long-term *in vivo* performance. Investigations into long-term fatigue behavior under cyclic physiological loading and comprehensive *in vivo* studies are necessary to validate the clinical applicability of these alloys. Numerical modeling and simulation of melt pool dynamics and microstructure evolution could offer deeper insights into defect formation mechanisms and optimization pathways.

Bibliography

Abd-Elaziem, W., Darwish, M. A., Hamada, A. & Daoush, W. M. (2024). Titanium-Based alloys and composites for orthopedic implants Applications: A comprehensive review. In *Materials and Design* (Vol. 241). Elsevier Ltd. https://doi.org/10.1016/j.matdes.2024.112850

Akhtar, M., Razick, D., Jundi, M., Zahir, J., Aamer, S., Dhaliwal, A., Shelton, T. & Wang, D. (2025). Clinical Outcomes of Primary Versus Revision Hip Arthroscopic Surgery: A Systematic Review and Meta-analysis. *American Journal of Sports Medicine*. https://doi.org/10.1177/03635465251324944

Akman, A., Douest, Y., Alberta, L. A., Perrin, K., Trunfio Sfarghiu, A. M., Courtois, N., Ter-Ovanessian, B., Pilz, S., Zimmermann, M., Calin, M. & Gebert, A. (2024). Tribocorrosion behaviour of additively manufactured β-type Ti–Nb alloy for implant applications. *Journal of Materials Research and Technology*, *31*, 1419–1429. https://doi.org/10.1016/j.jmrt.2024.06.172

Araya, M., Jaskari, M., Rautio, T., Guillén, T. & Järvenpää, A. (2024). Assessing the compressive and tensile properties of TPMS-Gyroid and stochastic Ti64 lattice structures: A study on laser powder bed fusion manufacturing for biomedical implants. *Journal of Science: Advanced Materials and Devices*, *9*(1). https://doi.org/10.1016/j.jsamd.2023.100663

Arputharaj, J. D., Nafisi, S. & Ghomashchi, R. (2025). Compression Behaviour of L-PBF-Manufactured Ti6Al4V BCC Lattices. *Metals*, *15*(2). https://doi.org/10.3390/met15020220

ASTM international. (2022). *Test Methods for Tension Testing of Metallic Materials*. ASTM International. https://doi.org/10.1520/E0008_E0008M-22

ASTM International. (2025). *Test Methods of Compression Testing of Metallic Materials at Room Temperature*. ASTM International. https://doi.org/10.1520/E0009-19R25E01

Attar, H., Calin, M., Zhang, L. C., Scudino, S. & Eckert, J. (2014). Manufacture by selective laser melting and mechanical behavior of commercially pure titanium. *Materials Science and Engineering: A*, *593*, 170–177. https://doi.org/10.1016/j.msea.2013.11.038

Aydin, A., Cetin, E., Erman, S. C. & Mumtaz, K. (2025). Laser powder bed fusion of Ti6Al4V using low-cost high efficiency 450 nm diode point melting. *Journal of Materials Research and Technology*, *34*, 2814–2827. https://doi.org/10.1016/j.jmrt.2024.12.252

Bartolomeu, F., Gasik, M., Silva, F. S. & Miranda, G. (2022). Mechanical Properties of Ti6Al4V Fabricated by Laser Powder Bed Fusion: A Review Focused on the Processing and Microstructural Parameters Influence on the Final Properties. In *Metals* (Vol. 12, Issue 6). MDPI. https://doi.org/10.3390/met12060986

Batalha, R L, Pinotti, V. E., Alnoaimy, O. O. S., Batalha, W. C., Gustmann, T., Kosiba, K., Pauly, S., Bolfarini, C., Kiminami, C. S. & Gargarella, P. (2022). Microstructure and properties of TiB2-reinforced Ti–35Nb–7Zr–5Ta processed by laser-powder bed fusion. *Journal of Materials Research*, *37*(1), 259–271. https://doi.org/10.1557/s43578-021-00422-z

Batalha, Rodolfo Lisboa, Batalha, W. C., Deng, L., Gustmann, T., Pauly, S., Kiminami, C. S. & Gargarella, P. (2020). Processing a biocompatible Ti-35Nb-7Zr-5Ta alloy by selective laser melting. *Journal of Materials Research*, *35*(9), 1143–1153. https://doi.org/10.1557/jmr.2020.90

Batalha, W. C., Batalha, R. L., Kosiba, K., Kiminami, C. S. & Gargarella, P. (2023a). Effect of scanning strategy on microstructure and mechanical properties of a biocompatible Ti–35Nb–7Zr–5Ta alloy processed by laser-powder bed fusion. *Journal of Materials Research*, *38*(1), 154–164. https://doi.org/10.1557/s43578-022-00735-7

Batalha, W. C., Batalha, R. L., Kosiba, K., Kiminami, C. S. & Gargarella, P. (2023b). Effect of scanning strategy on microstructure and mechanical properties of a biocompatible Ti–35Nb–7Zr–5Ta alloy processed by laser-powder bed fusion. *Journal of Materials Research*, *38*(1), 154–164. https://doi.org/10.1557/s43578-022-00735-7

Bönisch, M. R. N. M. (2016). *Structural properties, deformation behavior and thermal stability of martensitic Ti-Nb alloys*. https://doi.org/https://www.researchgate.net/publication/319873981_Structural_properties_deformation_behavior_and_thermal_stability_of_martensitic_Ti-Nb_alloys

Bora, R., Shukla, M. & Kumar, A. (2023). Finite element analysis based design of biomimetic functionally graded Ti-6Al-4V alloy scaffolds for human cortical bone applications. *Materials Today: Proceedings*, *90*, 81–85. https://doi.org/10.1016/j.matpr.2023.05.057

Bordbar-Khiabani, A. & Gasik, M. (2023). Electrochemical and biological characterization of Ti–Nb–Zr–Si alloy for orthopedic applications. *Scientific Reports*, *13*(1). https://doi.org/10.1038/s41598-023-29553-5

Brodie, E. G., Richter, J., Wegener, T., Niendorf, T. & Molotnikov, A. (2020). Low-cycle fatigue performance of remelted laser powder bed fusion (L-PBF) biomedical Ti25Ta. *Materials Science and Engineering: A*, *798*. https://doi.org/10.1016/j.msea.2020.140228

Cao, S., Zou, Y., Lim, C. V. S. & Wu, X. (2021). Review of laser powder bed fusion (LPBF) fabricated Ti-6Al-4V: process, post-process treatment, microstructure, and property. *Light: Advanced Manufacturing*, *2*(3). https://doi.org/10.37188/lam.2021.020

Chen, D., Li, D., Pan, K., Gao, S., Wang, B., Sun, M., Zhao, C., Liu, X. & Li, N. (2022). Strength enhancement and modulus modulation in auxetic meta-biomaterials produced by selective laser melting. *Acta Biomaterialia*, *153*, 596–613. https://doi.org/10.1016/j.actbio.2022.09.045

Chen, Z., Yan, X., Yin, S., Liu, L., Liu, X., Zhao, G., Ma, W., Qi, W., Ren, Z., Liao, H., Liu, M., Cai, D. & Fang, H. (2020). Influence of the pore size and porosity of selective laser melted Ti6Al4V ELI porous scaffold on cell proliferation, osteogenesis and bone ingrowth. *Materials Science and Engineering C*, *106*. https://doi.org/10.1016/j.msec.2019.110289

Cheng, A., Humayun, A., Cohen, D. J., Boyan, B. D. & Schwartz, Z. (2014). Additively manufactured 3D porous Ti-6Al-4V constructs mimic trabecular bone structure and regulate osteoblast proliferation, differentiation and local factor production in a porosity and surface roughness dependent manner. *Biofabrication*, *6*(4). https://doi.org/10.1088/1758-5082/6/4/045007

Cheng, H. H., Ma, H. W., Pan, L. ling, Luo, X., Liu, L. hua, Dong, H. K., Song, T., Wang, F. & Yang, C. (2024). Manufacturability and mechanical properties of Ti-35Nb-7Zr-5Ta porous titanium alloys produced by laser powder-bed fusion. *Additive Manufacturing*, *86*. https://doi.org/10.1016/j.addma.2024.104190

Chmielewska, A. & Dean, D. (2024). The role of stiffness-matching in avoiding stress shielding-induced bone loss and stress concentration-induced skeletal reconstruction device failure. In *Acta Biomaterialia* (Vol. 173, pp. 51–65). Acta Materialia Inc. https://doi.org/10.1016/j.actbio.2023.11.011

Chowdhury, S., Yadaiah, N., Prakash, C., Ramakrishna, S., Dixit, S., Gupta, L. R. & Buddhi, D. (2022). Laser powder bed fusion: a state-of-the-art review of the technology, materials, properties & defects, and numerical modelling. *Journal of Materials Research and Technology*, *20*, 2109–2172. https://doi.org/https://doi.org/10.1016/j.jmrt.2022.07.121

Colombo-Pulgarín, J. C., Biffi, C. A., Vedani, M., Celentano, D., Sánchez-Egea, A., Boccardo, A. D. & Ponthot, J. P. (2021). Beta Titanium Alloys Processed By Laser Powder Bed Fusion: A Review. In *Journal of Materials Engineering and Performance* (Vol. 30, Issue 9, pp. 6365–6388). Springer. https://doi.org/10.1007/s11665-021-05800-6

Dabaja, R., Swanson, W. B., Bak, S.-Y., Mendonca, G., Mishina, Y. & Banu, M. (2025). Spatially distributed and interconnected porous architectures for dental implants. *International Journal of*

Implant Dentistry, *11*(1). https://doi.org/10.1186/s40729-025-00618-6

David Deus Vilhena, I. DE. (2022). *ADDITIVE MANUFACTURING OF METALLIC AUXETIC STRUCTURES FOR BIOMEDICAL APPLICATIONS*. https://www.proquest.com/openview/2bb86f259a3e633a6242f2a49ea5cb83/1?pq-origsite=gscholar&cbl=2026366&diss=y

Delpazir, M. H., Asherloo, M., Nasiri Khalil Abad, S., Thompson, A., Guma, V., Bagi, S. D., Sreenivas, K. K., Paliwal, M., Terry, J., Rollett, A. D. & Mostafaei, A. (2023). Microstructure and corrosion behavior of differently heat-treated Ti-6Al-4V alloy processed by laser powder bed fusion of hydride-dehydride powder. *Corrosion Science*, *224*. https://doi.org/10.1016/j.corsci.2023.111495

Deng, B., Tang, X., Zhang, D., Dai, Y., Lin, J., Tong, X., Li, Y., Lin, J. & Wen, C. (2025). Compression fatigue behavior of gyroid porous titanium scaffolds manufactured by laser powder bed fusion for bone-implant applications. *International Journal of Fatigue*, *201*. https://doi.org/10.1016/j.ijfatigue.2025.109136

Deng, T., Li, M., Gong, S., Chen, P., Wang, J., Zhang, H., Wang, B., Wu, Z., Li, K. & Nie, Y. (2025). Voronoi as the optimal approach for strut-based bone scaffold design. *International Journal of Mechanical Sciences*, *295*. https://doi.org/10.1016/j.ijmecsci.2025.110124

Derimow, N., Benzing, J. T., Garcia, J., Levin, Z. S., Lu, P., Moser, N., Beamer, C., Delrio, F. W. & Hrabe, N. (2025). *Precipitation hardening of laser powder bed fusion Ti-6Al-4V*. https://doi.org/10.1016/j.msea.2024.147549

Dwivedi, M. (2025). Manufacturing Letters Effect of build orientation on mechanical and physical properties of Ti-6Al-4V L-PBF additively manufactured thin structures without support. In *Manufacturing Letters* (Vol. 44). https://doi.org/10.1016/j.mfglet.2025.06.110

Fan, H., Wang, C., Tian, Y., Zhou, K. & Yang, S. (2023). Laser powder bed fusion (L-PBF) of Ti–6Al–4V/Ti–6Al–2Sn–4Zr–2Mo and Ti–6Al–4V/γ-TiAl bimetals: Processability, interface and mechanical properties. *Materials Science and Engineering: A*, *871*. https://doi.org/10.1016/j.msea.2023.144907

Gandhi, R., Salmi, M., Roy, B., Pauli, L., Pagliari, L. & Concli, F. (2025). Mechanical and fatigue performance of multidirectional functionally graded Ti6Al4V scaffolds produced via laser powder bed fusion for orthopedic implants. *Materials and Design*, *251*. https://doi.org/10.1016/j.matdes.2025.113725

Gökçe, A., Balla, V. K., Nath, S. D., Akilan, A. A. & Atre, S. V. (2025). Laser Powder Bed Fusion of a

Ti-16Nb-Based Alloy: Processability, Microstructure, and Mechanical Properties. *Metals*, *15*(7). https://doi.org/10.3390/met15070728

González-Guillén, C., Romero-Resendiz, L., Naeem, M., Vidilli, A. L., Otani, L. B., Klyatskina, E., Gonzalez, G. & Amigó, V. (2024). Microstructural and mechanical behavior of second-phase hardened porous refractory Ti-Nb-Zr-Ta alloys. *Journal of Alloys and Compounds*, *980*. https://doi.org/10.1016/j.jallcom.2024.173605

Gu, D., Hagedorn, Y. C., Meiners, W., Meng, G., Batista, R. J. S., Wissenbach, K. & Poprawe, R. (2012). Densification behavior, microstructure evolution, and wear performance of selective laser melting processed commercially pure titanium. *Acta Materialia*, *60*(9), 3849–3860. https://doi.org/10.1016/j.actamat.2012.04.006

Hafeez, N., Wei, D., Xie, L., Tang, Y., Liu, J., Kato, H., Lu, W., Zhang, L.-C. & Wang, L. (2021). Evolution of microstructural complex transitions in low-modulus β-type Ti-35Nb-2Ta-3Zr alloy manufactured by laser powder bed fusion. *Additive Manufacturing*, *48*, 102376. https://doi.org/https://doi.org/10.1016/j.addma.2021.102376

Herath, B., Suresh, S., Downing, D., Cometta, S., Tino, R., Castro, N. J., Leary, M., Schmutz, B., Wille, M. L. & Hutmacher, D. W. (2021). Mechanical and geometrical study of 3D printed Voronoi scaffold design for large bone defects. *Materials and Design*, *212*. https://doi.org/10.1016/j.matdes.2021.110224

Herzog, D., Seyda, V., Wycisk, E. & Emmelmann, C. (2016). Additive manufacturing of metals. *Acta Materialia*, *117*, 371–392. https://doi.org/10.1016/j.actamat.2016.07.019

Huber, F., Papke, T., Kauffmann, C., Rothfelder, R., Krakhmalev, P., Merklein, M. & Schmidt, M. (2021). Systematic exploration of the L-PBF processing behavior and resulting properties of β-stabilized Ti-alloys prepared by in-situ alloy formation. *Materials Science and Engineering: A*, *818*, 141374. https://doi.org/https://doi.org/10.1016/j.msea.2021.141374

Ibrahim, P., Garrard, R. & Attallah, M. M. (2024). Laser powder bed fusion of a β titanium alloy: Microstructural development, post-processing, and mechanical behaviour. *Materials Science and Engineering: A*, *905*. https://doi.org/10.1016/j.msea.2024.146617

Issariyapat, A., Huang, J., Teramae, T., Kariya, S., Bahador, A., Visuttipitukul, P., Umeda, J., Alhazaa, A. & Kondoh, K. (2023). Microstructure refinement and strengthening mechanisms of additively manufactured Ti-Zr alloys prepared from pre-mixed feedstock. *Additive Manufacturing*, *73*. https://doi.org/10.1016/j.addma.2023.103649

Jamshidi, P., Aristizabal, M., Kong, W., Villapun, V., Cox, S. C., Grover, L. M. & Attallah, M. M. (2020). Selective laser melting of ti-6al-4v: The impact of post-processing on the tensile, fatigue and biological properties for medical implant applications. *Materials*, *13*(12), 1–16. https://doi.org/10.3390/ma13122813

Johannsen, J., Lauhoff, C., Stenzel, M., Schnitter, C., Niendorf, T. & Weinmann, M. (2023). Laser beam powder bed fusion of novel biomedical titanium/niobium/tantalum alloys: Powder synthesis, microstructure evolution and mechanical properties. *Materials and Design*, *233*. https://doi.org/10.1016/j.matdes.2023.112265

Kong, W., Cox, S. C., Lu, Y., Villapun, V., Xiao, X., Ma, W., Liu, M. & Attallah, M. M. (2021a). The influence of zirconium content on the microstructure, mechanical properties, and biocompatibility of in-situ alloying Ti-Nb-Ta based β alloys processed by selective laser melting. *Materials Science and Engineering: C*, *131*, 112486. https://doi.org/https://doi.org/10.1016/j.msec.2021.112486

Kong, W., Cox, S. C., Lu, Y., Villapun, V., Xiao, X., Ma, W., Liu, M. & Attallah, M. M. (2021b). The influence of zirconium content on the microstructure, mechanical properties, and biocompatibility of in-situ alloying Ti-Nb-Ta based β alloys processed by selective laser melting. *Materials Science and Engineering C*, *131*. https://doi.org/10.1016/j.msec.2021.112486

Li, J., Yang, Y., Sun, Z., Peng, K., Liu, K., Xu, P., Li, J., Wei, X. & He, X. (2024). Integrated evaluation of biomechanical and biological properties of the biomimetic structural bone scaffold: Biomechanics, simulation analysis, and osteogenesis. *Materials Today Bio*, *24*. https://doi.org/10.1016/j.mtbio.2023.100934

Li, Yongyue, Liu, Y., Chen, H., Zhang, A., Zhang, Y., Zhang, J., Chen, B., Han, Q. & Wang, J. (2024). From clinic to lab: Advances in porous titanium-based orthopedic implant research. *Journal of Materials Research and Technology*, *30*, 3780–3806. https://doi.org/10.1016/j.jmrt.2024.04.136

Li, Yue, Wang, L., Wu, H., Ding, F., Lei, M., Yang, J., Oliveira, J. P., Yan, M., Guo, W. & Li, Y. (2026). High strength, low modulus, and ductile metastable beta Ti-Nb-Zr-Fe alloys by laser powder bed fusion in-situ alloying. *Journal of Materials Science and Technology*, *241*, 270–283. https://doi.org/10.1016/j.jmst.2025.02.083

Lisboa Batalha, R. (2019). *SELECTIVE LASER MELTING OF A BIOCOMPATIBLE Ti-35Nb-7Zr-5Ta ALLOY (Doctoral Thesis), Federal University Of São Carlos*. https://doi.org/10.13140/RG.2.2.30991.20642

Liu, H., Li, Y., Fang, M., Han, Y., Chai, X., Peng, S., Zhang, T., Peng, L. & Lu, W. (2023). Tailoring microstructure with special bimodal structure to improve the ductility and fatigue life of laser powder bed fused Ti6Al4V alloy. *Materials Science and Engineering: A*, *878*. https://doi.org/10.1016/j.msea.2023.145234

Ma, H. Y., Wang, J. C., Qin, P., Liu, Y. J., Chen, L. Y., Wang, L. Q. & Zhang, L. C. (2024). Advances in additively manufactured titanium alloys by powder bed fusion and directed energy deposition: Microstructure, defects, and mechanical behavior. In *Journal of Materials Science and Technology* (Vol. 183, pp. 32–62). Chinese Society of Metals. https://doi.org/10.1016/j.jmst.2023.11.003

Ma, Y., Wang, Y., Tong, S., Wang, Y., Wang, Z., Sui, R., Yang, K., Witte, F. & Yang, S. (2024). Porous metal materials for applications in orthopedic field: A review on mechanisms in bone healing. *Journal of Orthopaedic Translation*, *49*, 135–155. https://doi.org/https://doi.org/10.1016/j.jot.2024.08.003

Marin, E. & Lanzutti, A. (2024). Biomedical Applications of Titanium Alloys: A Comprehensive Review. In *Materials* (Vol. 17, Issue 1). Multidisciplinary Digital Publishing Institute (MDPI). https://doi.org/10.3390/ma17010114

McConnell, S., Beshay, Y., Kourousis, K. & Tanner, D. (2025). Increasing productivity for laser powder bed fusion of Ti–6Al–4V parts through increased layer thickness. *Progress in Additive Manufacturing*. https://doi.org/10.1007/s40964-025-01079-4

McGregor, M., Patel, S., McLachlin, S. & Mihaela Vlasea. (2021). Architectural bone parameters and the relationship to titanium lattice design for powder bed fusion additive manufacturing. In *Additive Manufacturing* (Vol. 47). Elsevier B.V. https://doi.org/10.1016/j.addma.2021.102273

Memu, F., Durlu, N. & Yagmur, A. (2025). The Effect of Laser Powder Bed Fusion Process on Ti-6Al-4V Powder. *JOM*, *77*(5), 3906–3917. https://doi.org/10.1007/s11837-025-07217-1

Mohamed, O. F., Ismail, L., Verma, C., Barsoum, I., AlFantazi, A. & Schiffer, A. (2025). Microstructure and corrosion resistance of hybrid additively manufactured Ti-6Al-4V via laser powder bed fusion. *Scientific Reports*, *15*(1). https://doi.org/10.1038/s41598-025-16282-0

Nadammal, N., Rajput, M., Gupta, S. K., Ivanov, E., Reddy, A. S., Suwas, S. & Chatterjee, K. (2022). Laser Powder Bed Fusion Additive Manufacturing of a Low-Modulus Ti-35Nb-7Zr-5Ta Alloy for Orthopedic Applications. *ACS Omega*, *7*(10), 8506–8517. https://doi.org/10.1021/acsomega.1c06261

Nandhakumar, R. & Venkatesan, K. (2023). A process parameters review on selective laser melting-based additive manufacturing of single and multi-material: Microstructure, physical properties, tribological, and surface roughness. *Materials Today Communications*, *35*, 105538.

https://doi.org/https://doi.org/10.1016/j.mtcomm.2023.105538

National Joint Registry. (2024, 1. April). *NJR Annual Report* . NJR Annual Report . https://www.njrcentre.org.uk/

Ni, C., Zhu, J., Zhang, B., An, K., Wang, Y., Liu, D., Lu, W., Zhu, L. & Liu, C. (2025). Recent advance in laser powder bed fusion of Ti–6Al–4V alloys: microstructure, mechanical properties and machinability. In *Virtual and Physical Prototyping* (Vol. 20, Issue 1). Taylor and Francis Ltd. https://doi.org/10.1080/17452759.2024.2446952

Noronha, J., Rogers, J., Leary, M., Kyriakou, E., Inverarity, S. B., Das, R., Brandt, M. & Qian, M. (2023). Ti-6Al-4V hollow-strut lattice materials by laser powder bed fusion. *Additive Manufacturing*, *72*. https://doi.org/10.1016/j.addma.2023.103637

Oliveira, J. P., LaLonde, A. D. & Ma, J. (2020). Processing parameters in laser powder bed fusion metal additive manufacturing. *Materials & Design*, *193*, 108762. https://doi.org/https://doi.org/10.1016/j.matdes.2020.108762

Pan, C., Han, Y. & Lu, J. (2020). Design and optimization of lattice structures: A review. In *Applied Sciences (Switzerland)* (Vol. 10, Issue 18, pp. 1–36). MDPI AG. https://doi.org/10.3390/APP10186374

Papazoglou, D. P., Neidhard-Doll, A. T., Pinnell, M. F., Erdahl, D. S. & Osborn, T. H. (2024). Compression and Tensile Testing of L-PBF Ti-6Al-4V Lattice Structures with Biomimetic Porosities and Strut Geometries for Orthopedic Implants. *Metals*, *14*(2). https://doi.org/10.3390/met14020232

Peng, X., Li, S., He, D., Li, J., Qu, S. & Jin, Z. (2024). Expanding the mechanical and mass-transport combination for bone scaffolds: Through stretched structure. *Composite Structures*, *329*. https://doi.org/10.1016/j.compstruct.2023.117783

Penny, R. W., Kutschke, Z. & Hart, A. J. (2025). High-fidelity optical monitoring of laser powder bed fusion via aperture division multiplexing. *Npj Advanced Manufacturing*, *2*(1). https://doi.org/10.1038/s44334-025-00039-8

Pesode, P. & Barve, S. (2023). A review—metastable β titanium alloy for biomedical applications. In *Journal of Engineering and Applied Science* (Vol. 70, Issue 1). Institute for Ionics. https://doi.org/10.1186/s44147-023-00196-7

Pilz, S., Bönisch, M., Datye, A., Zhang, S., Günther, F., Drescher, S., Kühn, U., Schwarz, U. D., Zimmermann, M. & Gebert, A. (2024). Tailoring microstructure and mechanical properties of an LPBF-processed beta Ti-Nb alloy through post-heat treatments. *Materials and Design*, *239*. https://doi.org/10.1016/j.matdes.2024.112799

Pilz, Stefan, Gustmann, T., Günther, F., Zimmermann, M., Kühn, U. & Gebert, A. (2022). Controlling the Young's modulus of a ß-type Ti-Nb alloy via strong texturing by LPBF. *Materials and Design*, *216*. https://doi.org/10.1016/j.matdes.2022.110516

Rehman, M., Wang, Y., Ishfaq, K., Mushtaq, R. T. & Alkahtani, M. (2024). A novel methodology for developing dense and porous implants on single generic optimized setting for excellent bio-mechanical characteristics. *Journal of Materials Research and Technology*, *33*, 2593–2611. https://doi.org/10.1016/j.jmrt.2024.09.209

Rehman, M., Wang, Y., Ishfaq, K., Mushtaq, R. T., Khan, A. M., Alkahtani, M., Nazir, A. & Afzal, M. (2025). A comparative bio-mechanical performance assessment of additively manufactured bone scaffolds using different beta Ti alloys and Gyroid based cellular structure. *Journal of Materials Research and Technology*, *35*, 1565–1585. https://doi.org/10.1016/j.jmrt.2025.01.096

Rehman, M., Wang, Y., Ishfaq, K., Mushtaq, R. T., Kumar, M. S. & Yang, H. (2023). Potential assessment in laser powder bed fusion of bionic porous Ti scaffolds concerning compressive behavior, porosity, and surface roughness. *Journal of Manufacturing Processes*, *95*, 461–478. https://doi.org/https://doi.org/10.1016/j.jmapro.2023.04.030

Schulze, C., Weinmann, M., Schweigel, C., Keßler, O. & Bader, R. (2018). Mechanical properties of a newly additive manufactured implant material based on Ti-42Nb. *Materials*, *11*(1). https://doi.org/10.3390/ma11010124

Seehanam, S., Khrueaduangkham, S., Sinthuvanich, C., Sae-Ueng, U., Srimaneepong, V. & Promoppatum, P. (2024). Evaluating the effect of pore size for 3d-printed bone scaffolds. *Heliyon*, *10*(4). https://doi.org/10.1016/j.heliyon.2024.e26005

Sefene, E. M. (2022). State-of-the-art of selective laser melting process: A comprehensive review. *Journal of Manufacturing Systems*, *63*, 250–274. https://doi.org/https://doi.org/10.1016/j.jmsy.2022.04.002

Senftleben, F., Calin, M., Eckert, J. & Bönisch, M. (2025). Laser powder bed fusion vs. single track laser melting of martensitic Ti-Nb: Phase and microstructure formation. *Additive Manufacturing*, *109*. https://doi.org/10.1016/j.addma.2025.104884

Sheremetyev, V., Konopatsky, A., Teplyakova, T., Lezin, V., Lukashevich, K., Derkach, M., Kostyleva, A., Koudan, E., Permyakova, E., Iakimova, T., Boychenko, O., Klyachko, N., Shtansky, D., Prokoshkin, S. & Brailovski, V. (2024). Surface modification of the laser powder bed-fused Ti-Zr-Nb scaffolds by dynamic chemical etching and Ag nanoparticles decoration. *Biomaterials Advances*, *161*. https://doi.org/10.1016/j.bioadv.2024.213882

Shuvho, M. B. A., Juri, A. Z., Basak, A. K., Kotousov, A. & Yin, L. (2025). Micromechanical characteristics of titanium alloy (Ti-6Al-4V) made by laser powder bed fusion using an in-situ SEM micropillar compression technique. *Journal of the Mechanical Behavior of Biomedical Materials*, *161*. https://doi.org/10.1016/j.jmbbm.2024.106794

Simonelli, M., Tse, Y. Y. & Tuck, C. (2014). On the texture formation of selective laser melted Ti-6Al-4V. *Metallurgical and Materials Transactions A: Physical Metallurgy and Materials Science*, *45*(6), 2863–2872. https://doi.org/10.1007/s11661-014-2218-0

Singla, A. K., Banerjee, M., Sharma, A., Singh, J., Bansal, A., Gupta, M. K., Khanna, N., Shahi, A. S. & Goyal, D. K. (2021). Selective laser melting of Ti6Al4V alloy: Process parameters, defects and post-treatments. In *Journal of Manufacturing Processes* (Vol. 64, pp. 161–187). Elsevier Ltd. https://doi.org/10.1016/j.jmapro.2021.01.009

SITI NUR HAZWANI, M. R., LIM, L. X., LOCKMAN, Z. & ZUHAILAWATI, H. (2022). Fabrication of titanium-based alloys with bioactive surface oxide layer as biomedical implants: Opportunity and challenges. *Transactions of Nonferrous Metals Society of China (English Edition)*, *32*(1), 1–44. https://doi.org/10.1016/S1003-6326(21)65776-X

Soltani-Tehrani, A., Isaac, J. P., Tippur, H. V., Silva, D. F., Shao, S. & Shamsaei, N. (2023). Ti-6Al-4V powder reuse in laser powder bed fusion (L-PBF): The effect on porosity, microstructure, and mechanical behavior. *International Journal of Fatigue*, *167*. https://doi.org/10.1016/j.ijfatigue.2022.107343

Squillaci, L., Neikter, M., Hansson, T., Pederson, R. & Moverare, J. (2025). Microstructure and mechanical properties of Ti-6Al-4V alloy fabricated using powder bed fusion – laser beam additive manufacturing process: Effect of hot isostatic pressing. *Materials Science and Engineering: A*, *931*. https://doi.org/10.1016/j.msea.2025.148226

Subramanian, S., Yadav, M. K., Jayaraj, J., Yangyang, F., Xi, L. & Prashanth, K. G. (2025). Microstructural homogenization through laser remelting in an additively manufactured Ti–40Nb sample from elemental feedstock powders. *Journal of Materials Research and Technology*, *38*, 4305–4320. https://doi.org/10.1016/j.jmrt.2025.08.203

Tang, H., Li, R., Wang, F., Lin, S. & Yuan, T. (2024). Effect of Zr on the morphology, microstructure and mechanical properties of NbTa0.5TiZrX refractory high entropy alloy fabricated by selective laser melting. *Materials Characterization*, *209*. https://doi.org/10.1016/j.matchar.2024.113676

Tardelli, J. D. C., Valente, M. L. da C., Otani, L. B., Batalha, R. L., Alves, F., Pereira-da-Siva, M. A., Bagnato, V. S., Dibb, R. G. P., Gargarella, P., Bolfarini, C. & Reis, A. C. dos. (2024a). Analysis of physical, chemical, mechanical, and microbiological properties of Ti–35Nb–7Zr–5Ta and Ti–6Al–4V discs obtained by machining and additive manufacturing. *Ceramics International*, *50*(2, Part A), 2845–2854. https://doi.org/https://doi.org/10.1016/j.ceramint.2023.11.008

Tardelli, J. D. C., Valente, M. L. da C., Otani, L. B., Batalha, R. L., Alves, F., Pereira-da-Siva, M. A., Bagnato, V. S., Dibb, R. G. P., Gargarella, P., Bolfarini, C. & Reis, A. C. dos. (2024b). Analysis of physical, chemical, mechanical, and microbiological properties of Ti–35Nb–7Zr–5Ta and Ti–6Al–4V discs obtained by machining and additive manufacturing. *Ceramics International*, *50*(2), 2845–2854. https://doi.org/10.1016/j.ceramint.2023.11.008

Terrazas-Najera, C. A., Mayoral, F. L., Garcia, O. F., Hossain, M. S., Espalin, D., Fernandez, A., Murr, L. E. & Wicker, R. B. (2021). Effects of process interruptions on microstructure and mechanical properties of three face centered cubic alloys processed by laser powder bed fusion. *Journal of Manufacturing Processes*, *66*, 397–406. https://doi.org/https://doi.org/10.1016/j.jmapro.2021.04.013

Tyagi, S. A. & M, M. (2023). Additive manufacturing of titanium-based lattice structures for medical applications – A review. *Bioprinting*, *30*, e00267. https://doi.org/https://doi.org/10.1016/j.bprint.2023.e00267

Umbelino dos Santos, L., Campo, K. N., Caram, R. & Najar Lopes, É. S. (2021). Oxygen addition in biomedical Ti–Nb alloys with low Nb contents: Effect on the microstructure and mechanical properties. *Materials Science and Engineering: A*, *823*. https://doi.org/10.1016/j.msea.2021.141750

Ummethala, R., Karamched, P. S., Rathinavelu, S., Singh, N., Aggarwal, A., Sun, K., Ivanov, E., Kollo, L., Okulov, I., Eckert, J. & Prashanth, K. G. (2020). Selective laser melting of high-strength, low-modulus Ti–35Nb–7Zr–5Ta alloy. *Materialia*, *14*. https://doi.org/10.1016/j.mtla.2020.100941

Vrancken, B., Thijs, L., Kruth, J. P. & Van Humbeeck, J. (2012). Heat treatment of Ti6Al4V produced by Selective Laser Melting: Microstructure and mechanical properties. *Journal of Alloys and Compounds*, *541*, 177–185. https://doi.org/10.1016/j.jallcom.2012.07.022

Wang, D., Han, H., Sa, B., Li, K., Yan, J., Zhang, J., Liu, J., He, Z., Wang, N. & Yan, M. (2022). A review and a statistical analysis of porosity in metals additively manufactured by laser powder bed fusion.

Opto-Electronic Advances, *5*(10). https://doi.org/10.29026/oea.2022.210058

Wang, J. C., Liu, Y. J., Liang, S. X., Zhang, Y. S., Wang, L. Q., Sercombe, T. B. & Zhang, L. C. (2022). Comparison of microstructure and mechanical behavior of Ti-35Nb manufactured by laser powder bed fusion from elemental powder mixture and prealloyed powder. *Journal of Materials Science and Technology*, *105*, 1–16. https://doi.org/10.1016/j.jmst.2021.07.021

Xiao, Y., Qian, G., Sun, J., Berto, F., Correia, J. A. F. & Hong, Y. (2023). Effects of temperature on tensile and fracture performance of Ti6Al4V alloy fabricated by laser powder bed fusion. *Theoretical and Applied Fracture Mechanics*, *125*. https://doi.org/10.1016/j.tafmec.2023.103931

Yu, G., Li, X., Dai, L., Xiao, L. & Song, W. (2022). Compressive properties of imperfect Ti-6Al-4V lattice structure fabricated by electron beam powder bed fusion under static and dynamic loadings. *Additive Manufacturing*, *49*. https://doi.org/10.1016/j.addma.2021.102497

Zhang, B., Wan, M., Gao, N., Jiang, H., Chen, T., Zhao, P., Liu, Z., Jiao, Q., Lv, B., Han, Q. & Wang, X. (2025). Influence of Nb Addition on the Microstructure and Mechanical Properties of Laser Powder Bed Fusion-Fabricated Ti6Al4V Alloy. *Materials*, *18*(8). https://doi.org/10.3390/ma18081803

Zhang, K., Wen, C., Wen, Z. & Lu, S. (2024). Effect of heat treatment on electrochemical behavior of biocompatible Ti–Ta–Nb–Zr alloys prepared by selective laser melting. *International Journal of Electrochemical Science*, *19*(9). https://doi.org/10.1016/j.ijoes.2024.100751

Zhang, L.-C., Chen, L.-Y., Zhou, S. & Luo, Z. (2023). Powder bed fusion manufacturing of beta-type titanium alloys for biomedical implant applications: A review. *Journal of Alloys and Compounds*, *936*, 168099. https://doi.org/https://doi.org/10.1016/j.jallcom.2022.168099

Zhao, D., Liang, H., Han, C., Li, J., Liu, J., Zhou, K., Yang, C. & Wei, Q. (2021). 3D printing of a titanium-tantalum Gyroid scaffold with superb elastic admissible strain, bioactivity and in-situ bone regeneration capability. *Additive Manufacturing*, *47*. https://doi.org/10.1016/j.addma.2021.102223

Zhou, C., Garcia, N., Pu, R., Sun, P. & Fang, Z. Z. (2025). Effect of Geometry on Local Microstructure in Ti-6Al-4V Fabricated by Laser Powder Bed Fusion. *Materials*, *18*(16). https://doi.org/10.3390/ma18163756

Zhou, L.-B., Shu, J.-G., Sun, J.-S., Chen, J., He, J.-J., Li, W., Huang, W.-Y., Niu, Y. & Yuan, T.-C. (2021). Effects of tantalum addition on microstructure and properties of titanium alloy fabricated by laser powder bed fusion. *Journal of Central South University*, *28*(4), 1111–1128. https://doi.org/10.1007/s11771-021-4684-z

Zhuo, Z., Ji, R., Wang, L. & Mao, J. (2025). Reusability of Ti-6Al-4V powder in laser powder bed fusion: Influence on powder morphology, oxygen uptake, and mechanical properties. *Journal of Materials Processing Technology*, *335*. https://doi.org/10.1016/j.jmatprotec.2024.118672

Zluhan, B., Ramadurga Narasimharaju, S., Cholkar, A., Thomas, K., Raghavendra, R. & Lopes, E. S. N. (2025). Design, defect analysis, compressive strength and surface texture characterization of Laser Powder Bed Fusion processed Ti6Al4V lattice structures. *Journal of Materials Research and Technology*, *35*, 2914–2933. https://doi.org/10.1016/j.jmrt.2025.01.232

Zou, Z., Dunstan, M. K., McWilliams, B., Hague, R. & Simonelli, M. (2024a). Identification of an affordable and printable metastable β Ti alloy with outstanding deformation behaviour for use in laser powder bed fusion. *Materials Science and Engineering: A*, *902*, 146619. https://doi.org/https://doi.org/10.1016/j.msea.2024.146619

Zou, Z., Dunstan, M. K., McWilliams, B., Hague, R. & Simonelli, M. (2024b). Identification of an affordable and printable metastable β Ti alloy with outstanding deformation behaviour for use in laser powder bed fusion. *Materials Science and Engineering: A*, *902*. https://doi.org/10.1016/j.msea.2024.146619